Photoacoustics 22 (2021) 100243

Contents lists available at ScienceDirect

Photoacoustics

journal homepage: www.elsevier.com/locate/pacs

Review article

Nonlinear mechanisms in photoacoustics—Powerful tools in photoacoustic imaging

Rongkang Gao, Zhiqiang Xu, Yaguang Ren, Liang Song, Chengbo Liu *

Research Laboratory for Biomedical Optics and Molecular Imaging, CAS Key Laboratory of Health Informatics, Shenzhen Institutes of Advanced Technology, Chinese Academy of Sciences, Shenzhen 518055, China

ARTICLE INFO

Keywords:
Nonlinearity
Photoacoustic imaging
Super-resolution
Super-imaging-contrast
Functional imaging
Parameter extraction

ABSTRACT

Many nonlinear effects have been discovered and developed in photoacoustic imaging. These nonlinear mechanisms have been explored for different utilizations, such as enhancing imaging contrast, measuring tissue temperature, achieving super-resolution imaging, enabling functional imaging, and extracting important physical parameters. This review aims to introduce different nonlinear mechanisms in photoacoustics, underline the fundamental principles, highlight their representative applications, and outline the occurrence conditions and applicable range of each nonlinear mechanism. Furthermore, this review thoroughly discusses the nonlinearity rule concerning how the mathematical structure of the nonlinear dependence is correlated to its practical applications. This summarization is useful for identifying and guiding the potential applications of nonlinearity based on their mathematical expressions, and is helpful for new nonlinear mechanism discovery or implementation in the future, which facilitates further breakthroughs in nonlinear photoacoustics.

1. Introduction

Photoacoustic (PA) technique, also referred to as the optoacoustic technique, is a revolutionary biomedical imaging method that provides structural and functional information of living biological tissues [1–4]. PA imaging incorporates optical illumination with ultrasound wave detection, extending the imaging depth limit of the conventional optical imaging method to the centimeter scale [5–7]. Hence, it has demonstrated significant potential in many pre-clinical and clinical practice, such as oncology [8,9], vascular biology [10,11], neurology [12–14], ion detection [6,15] and label-free functional imaging [16–18]. PA imaging is based on the PA effect, where biological tissues are illuminated by a non-ionizing pulsed laser beam and temporally confined optical absorption is converted into heat, resulting in a transient local temperature increase. The thermal-elastic expansion caused by the temperature rise, induces a pressure change with wideband ultrasonic emission and can be detected using an ultrasound transducer with amplitude, also termed as PA signals. It is known that the absorbed laser energy depends on the optical fluence (*F*) and physiological properties, such as the molar absorption coefficient and concentration of absorbers. Consequently, the magnitude of the PA signal generated by optical absorption is expressed as follows:

$$PA = k\Gamma\eta_{th}\mu_a F \tag{1}$$

where F indicates the local optical fluence (J/cm^2); μ_a is the absorption coefficient (cm^{-1}); η_{th} signifies the percentage of absorbed energy converted into heat; Γ denotes the Grueneisen parameter (dimensionless), which depicts the thermodynamic properties of absorbers; k is a constant related to detection sensitivity. Eq. (1) describes the behavior of PA signals of single-photon absorption under pulsed laser excitation. It is noteworthy that the pulse duration of optical laser needs to be much smaller than both the thermal and stress-relaxation times of a target [19,20] such that the thermal diffusion and pressure relaxation are negligible during the heat deposition of the laser illumination, which is the prerequisite for Eq. (1) to be used to determine the amplitude of the PA signal. Generally, nanosecond and picosecond pulsed lasers are typical excitation sources employed for PA imaging to satisfy both thermal and stress confinements. Herein, unless noted otherwise, it is assumed that both the thermal and stress confinements are satisfied in all cases discussed herein.

Conventionally, many photoacoustic studies assume a linear correlation between the PA amplitude and the optical fluence F, as well as between the PA amplitude and the absorption coefficient μ_a. However, these linear dependences may not be applicable to all cases. There are a number of conditions where the linear correlation no longer holds true and nonlinear

* Corresponding author.
E-mail address: cb.liu@siat.ac.cn (C. Liu).

https://doi.org/10.1016/j.pacs.2021.100243
Received 14 December 2020; Received in revised form 16 January 2021; Accepted 29 January 2021
Available online 1 February 2021

dependence occurs. So far, several types of nonlinear mechanisms have been investigated and developed, including absorption saturation-based nonlinearity [21–25], thermal-based nonlinearity [25–32], resolution-dependent nonlinearity [33–35], Grueneisen-relaxation-based nonlinearity [36–41], reversible-switching-based [42] and photobleaching-based nonlinearities [43]. Currently, these nonlinear effects have been applied to a wide range of applications, such as measuring tissue temperature [39], achieving super-resolution [36–38,42,43], discriminating between different absorbers [30], enhancing imaging contrast [37], enabling quantitative and functional imaging [24,34,44], and extracting important parameters such as absorption relaxation time [23]. Hence, these nonlinear phenomena have been revealed as a powerful tool in PA imaging.

Herein, we introduce the principles and recent progress of different nonlinear photoacoustics. Other nonlinear effects exist in PA imaging, such as nano-/microbubble generations [45,46], photochemical reactions [47], the photoacoustic resonance [48–51], unsatisfied stress and thermal confinement [52], and the nonlinear PA beamforming method [53–59]. However, we herein describe only the aforementioned six types of nonlinearity as representative examples. Though another review [60] has covered some of the nonlinear effects, this paper analyzes and explores the nonlinear mechanisms in a more physical and mathematical manner. The occurrence conditions of each nonlinear mechanism and their representative applications are outlined in the following section. Thereafter, we summarize the rules and common characteristics concerning the correlation between the mathematical structure of the nonlinear mechanism and different applications, providing insights into the potential utilization for the future progress of nonlinear photoacoustics.

2. The progress in nonlinear photoacoustics

This section summarizes different nonlinear effects, with a conceptual diagram of principles illustrated in Fig. 1. A detailed discussion of each nonlinear mechanism is provided in the following subsections.

2.1. Absorption saturation-based nonlinearity

2.1.1. Mechanism

The absorption coefficient μ_a is a product of the absorption cross-section σ_A and the number of absorbers per unit volume N_0, expressed as $\mu_a = \sigma_A N_0$. As indicated in Eq. (1), many photoacoustic studies assume a linear correlation between the PA amplitude and the optical fluence F by considering a constant absorption coefficient μ_a. However, this is applicable only when the optical intensities I (W/cm^2) are much lower than the saturation intensity I_{sat}. The laser intensity is proportional to the laser fluence $I = F/\tau_{laser}$, where τ_{laser} is the laser pulse width. Several studies have introduced and described the absorption saturation [21–24]. The optical absorption saturates with the increase in the pulse intensity in the following form [61]:

$$\mu_a(I) = \mu_{a0}\left(\frac{1}{1+I/I_{sat}}\right) = \sigma_{A0}N_0\left(\frac{1}{1+I/I_{sat}}\right), \tag{2}$$

where μ_{a0} and σ_{A0} denote the initial values of the absorption coefficient and absorption cross-section when the laser is not applied. This decreasing trend of μ_a with laser intensity is demonstrated in Fig. 1A. With a lower laser intensity ($I << I_{sat}$), $\mu_a(I) = \mu_{a0}$, no saturation occurs. When the intensity approaches I_{sat}, the absorption coefficient $\mu_a(I)$ decreases to half of its original value (μ_{a0}). I_{sat} is an inherent property of an absorber, expressed as [61]

$$I_{sat} = \frac{h\nu}{\sigma_{A0}\tau_{eff}}, \tag{3}$$

where h indicates Planck's constant, ν is the laser frequency, and τ_{eff} denotes the absorption relaxation time. The dependence of the PA signal on the local fluence is obtained by combining Eqs. (1) and (2),

$$PA = k\Gamma\eta_{th}\sigma_{A0}N_0\frac{1}{1+\frac{F}{\tau_{laser}I_{sat}}}F = k\Gamma\eta_{th}\sigma_{A0}N_0\tau_{laser}I_{sat}\left(1-\frac{1}{1+\frac{F}{\tau_{laser}I_{sat}}}\right) \tag{4}$$

Consequently, the PA signal demonstrates a negative reciprocal function correlation with F, the curve of which is shown in Fig. 2(A–D). At a lower range of F, the assumption of linear correlation between PA and F is still applicable because the negative reciprocal function can be regarded as a linear function. However, at a high range of F, the PA signal does not linearly reflect the increase in F but tends to converge to $k\Gamma\eta_{th}\sigma_{A0}N_0\tau_{laser}I_{sat}$ ($= k\Gamma\eta_{th}\mu_{a0}\tau_{laser}I_{sat}$). This value indicates that at extremely high fluence ranges, the PA dependence on the optical fluence F is completely removed, and the PA signal is only affected by the non-saturated absorption coefficient μ_{a0} when coefficients, k, Γ and η_{th} are constants.

2.1.2. Applications

2.1.2.1. Picosecond relaxation extraction. Absorption saturation-based nonlinearity can be employed to determine the absorption relaxation time τ_{eff} [23], which is a significant parameter in understanding the transient relaxation energy transfer processes as it relates to many photophysical and photochemical reactions, such as photosynthesis [62], photolysis [63] and transient changes in the molecular structure [64]. τ_{eff} is a picosecond-scale parameter and generally measured using the femto/picosecond pump-probe technique [65–69], which is not only costly but also susceptible to pulse broadening in dispersive media. Danielli et al. [23] applied the nonlinear mechanism to quantify τ_{eff} for the first time, where τ_{eff} is extracted by fitting the theoretical PA–F curve (Fig. 2, red line) to the measured PA–F curve (Fig. 2 black error bar) using τ_{eff} as a free parameter. The PA amplitude can be normalized to remove the requirement for parameters k, Γ and η_{th} to be known. The effectiveness of this approach was validated by measuring τ_{eff} of two known dyes (saturable absorber and DQOCI) and oxy/deoxygenated bovine blood (Fig. 2).

2.1.2.2. Single-wavelength functional photoacoustic microscopy (PAM). This nonlinear mechanism was also applied in the measurement of oxygen saturation *in vivo* with a single wavelength [24,44]. Oxygen saturation, defined as $sO_2 = N_{HbO_2}/(N_{HbO_2}+N_{HbR})$, is generally measured using a multi-wavelength approach [70–78] because PA spectroscopy is theoretically equivalent to the absorption spectroscopy in the wavelength dimension. Hence, the multi-wavelength approach, which generates multiple equations, can be adopted to solve the two unknown variables (N_{HbO_2} and N_{HbR}) in the following formula:

$$PA = k\Gamma\eta_{th}F\mu_a = k\Gamma\eta_{th}F\left(\sigma_{HbO_2}N_{HbO_2}+\sigma_{HbR}N_{HbR}\right), \tag{5}$$

where subscripts HbO_2 and HbR indicate oxy- and deoxy-hemoglobins, respectively. However, this approach suffers from the wavelength-dependent optical attenuation in biological tissues. The local fluence calibration in depth between wavelengths is still a challenge in PA imaging. The saturation-based nonlinear mechanism, interestingly, shows potentials to address this problem. When absorption saturation occurs, the PA signal as a function of N_{HbO_2} and N_{HbR} is expressed in the following formula [24], achieved by combining Eqs. (2) and (5).

$$PA(F) = k\Gamma\eta_{th}\left[\sigma_{HbO_2}\frac{N_{HbO_2}}{1+F/\left(\tau_{laser}\,I_{sat}^{HbO_2}\right)}F+\sigma_{HbR}\frac{N_{HbR}}{1+F/\left(\tau_{laser}\,I_{sat}^{HbR}\right)}F\right] \tag{6}$$

The saturation effect added another dimension to absorption spectroscopy, *i.e.*, the fluence dimension $\mu_a = \mu_a(\lambda, F)$, and also to PA

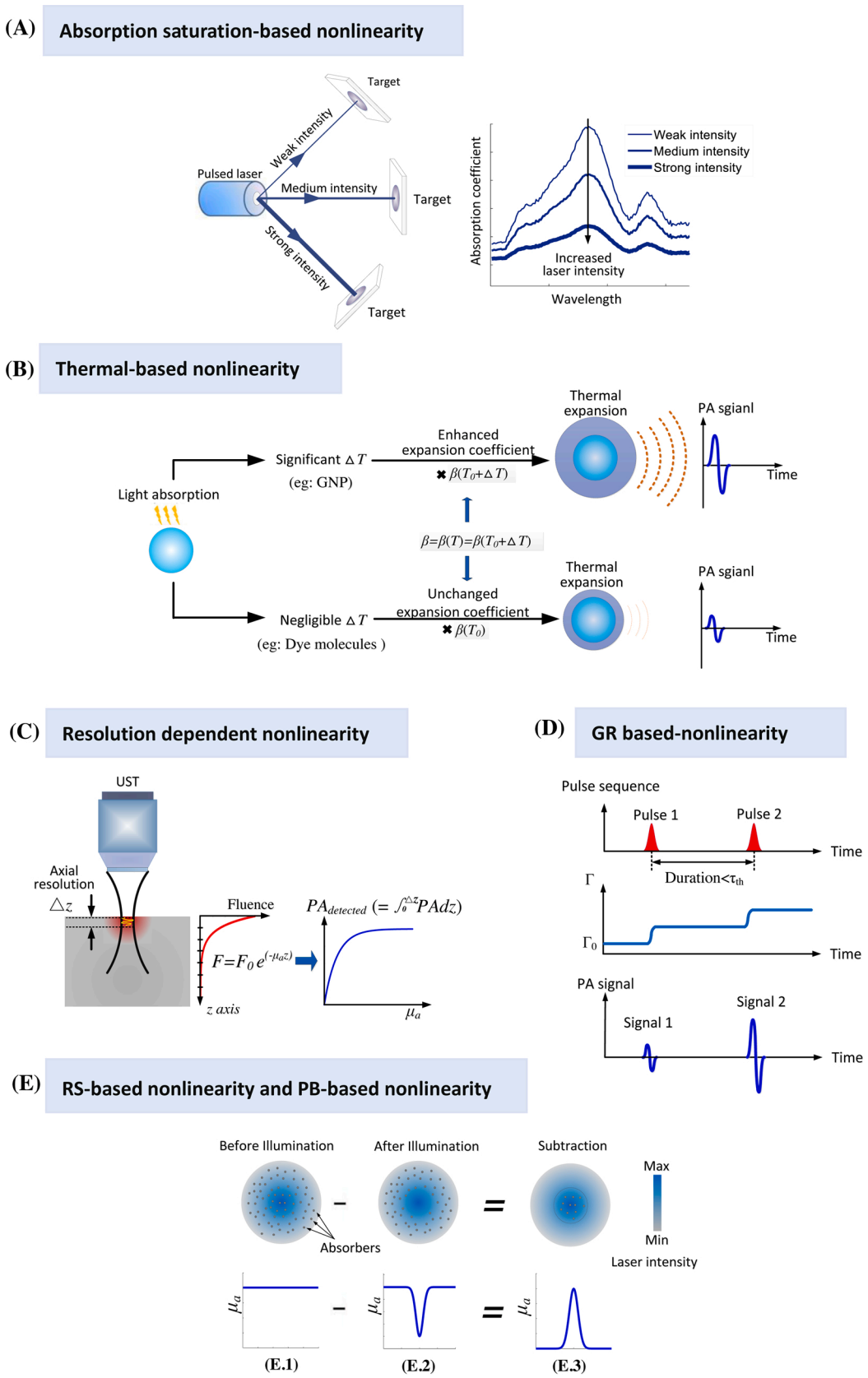

Fig. 1. Principle illustration of representative nonlinear mechanisms summarized herein. σ_A: absorption cross-section. GNP: gold nanoparticles. ΔT: transient temepratutre increase induced by pulsed laser. UST: ultrasound transducer. τ_{th}: thermal relaxation time. GR: Grueneisen-relaxation. τ_{th}: thermal relaxation time. RS: reversible switching. PB: photobleaching.

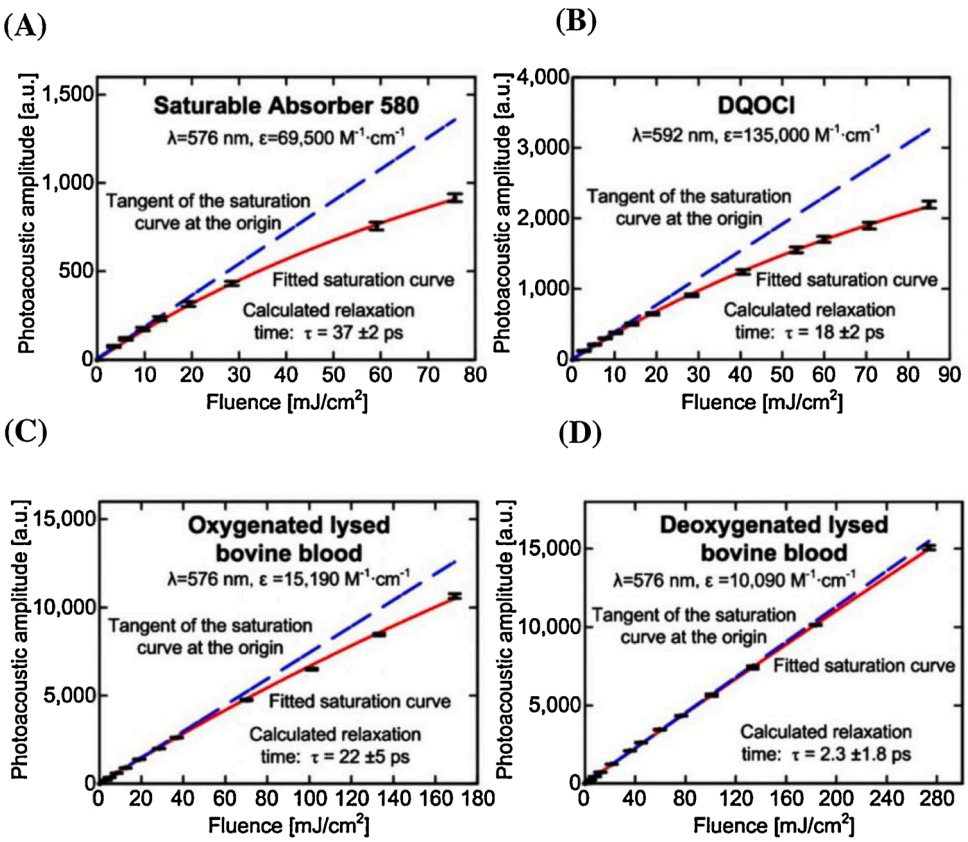

Fig. 2. PA–*F* curve fitting. **(A)** saturable absorber, **(B)** DQOCI dye, **(C)** oxygenated bovine blood, and **(D)** deoxygenated lysed bovine blood. Blue line: linear correlation; red line: nonlinear one. Figures reproduced with publisher's permission [23].

spectroscopy, *i.e.*, $PA = PA(\mu_a(\lambda,F),F)$, as reflected in Eq. (6). Based on this new dependence, different optical fluences produce different equations to solve the two unknown (N_{HbO_2} and N_{HbR}); hence, functional imaging of sO_2 can be achieved using a multi-fluence approach [24,44] rather than using the multi-wavelength approach. The validity of this technique was verified by imaging sO_2 in mouse ears (Fig. 3C), and the results agreed with multi-wavelength analyses (Fig. 3D) [24]. Fig. 3A and B shows the saturation profile at the vein and artery, indicated by white circles in Fig. 3C. The PA signal saturated faster in the artery than in the vein because HbO_2 has higher values of τ_{eff} and σ_A than HbR. In a recent study, Yao et al. [44] applied the signal wavelength method to quantify sO_2 based on different saturation properties between HbO_2 and HbR. Instead of employing a high optical fluence to reach the nonlinear regime, Yao et al. [44] used a picosecond laser to achieve absorption saturation with reduced laser fluence compared with nanosecond laser. Two laser systems, *i.e.*, nanosecond and picosecond systems, were used to differentiate HbO_2 and HbR with and without using the saturation effect, respectively. Hence, two equations, *i.e.*, $PA_{picosecond}$ following the form of Eq. (6) and $PA_{nanosecond}$ following the form of Eq. (5), were generated to solve two unknowns (N_{HbO_2} and N_{HbR}). Recently, another single-wavelength method is proposed in Ref [79]. This method uses a different approach—fusing optical absorption and scattering instead of absorption saturation-based nonlinearity, thus is not elaborated in this review.

The advantages of the single-wavelength method include (a) it eliminates the need for wavelength-dependent energy compensation; (b) it increases the imaging speed as no wavelength switching is employed; (c) it reduces the cost as only one single-wavelength laser source is required. However, this approach has its own limitations: (a) the imaging depth is restricted in this approach because the strong optical attenuation in biological tissues leads to a significant decrease of the local fluence, making it difficult to reach a nonlinear regime. The effective imaging depth is approximated to be around 0.5 mm at 532 nm, as reported in previous study [70]; (b) when using nanosecond laser, a high optical fluence is required to reach the nonlinear regime and may exceed the skin maximum permission exposure (MPE) to laser irradiation (20 mJ/cm^2 at 532 nm according to ANSI Z136.1-2014). This can also occur when employing a picosecond or femtosecond pulsed laser, in which case the MPE for skin exposure is assessed using the optical intensity (W/cm^2) [80].

Measuring sO_2 is one example of using the single-wavelength method. In a generic sense, this strategy has potentials to resolve any absorbers using their different saturation rates (τ_{eff} and σ_A) without calibrating the wavelength-dependent optical attenuation inside tissues. The feasibility of this approach is based on that the difference in saturation rate between different absorbers is significant enough to be resolved using the PA-*F* curve fitting. This approach may find more applications in the future, such as extracting targets from high-absorptive blood background, discriminating different tissues. More investigations are deserved to be performed towards real applications *in vivo*.

2.1.3. Occurrence conditions

In cases of intensifying the nonlinear degree to employ the nonlinearity mechanism for the applications above (Section 2.1.2), in addition to the increase in the optical fluence, the pulse duration of the laser τ_{laser} can be reduced to generate higher laser intensities, according to $I = F/\tau_{laser}$. Furthermore, according to $I_{sat} = h\nu/(\sigma_{A0}\tau_{eff})$, absorbing species with higher σ_{A0} and τ_{eff} result in a lower saturation threshold (I_{sat}) compared with the opposite condition (*i.e.*, absorbers with lower σ_{A0} and τ_{eff}), therefore the former (high σ_{A0} and τ_{eff} absorbers) more easily induces nonlinearity under the same condition than the latter (low σ_{A0} and τ_{eff} absorbers). By contrast, when a linear relation between the PA signal

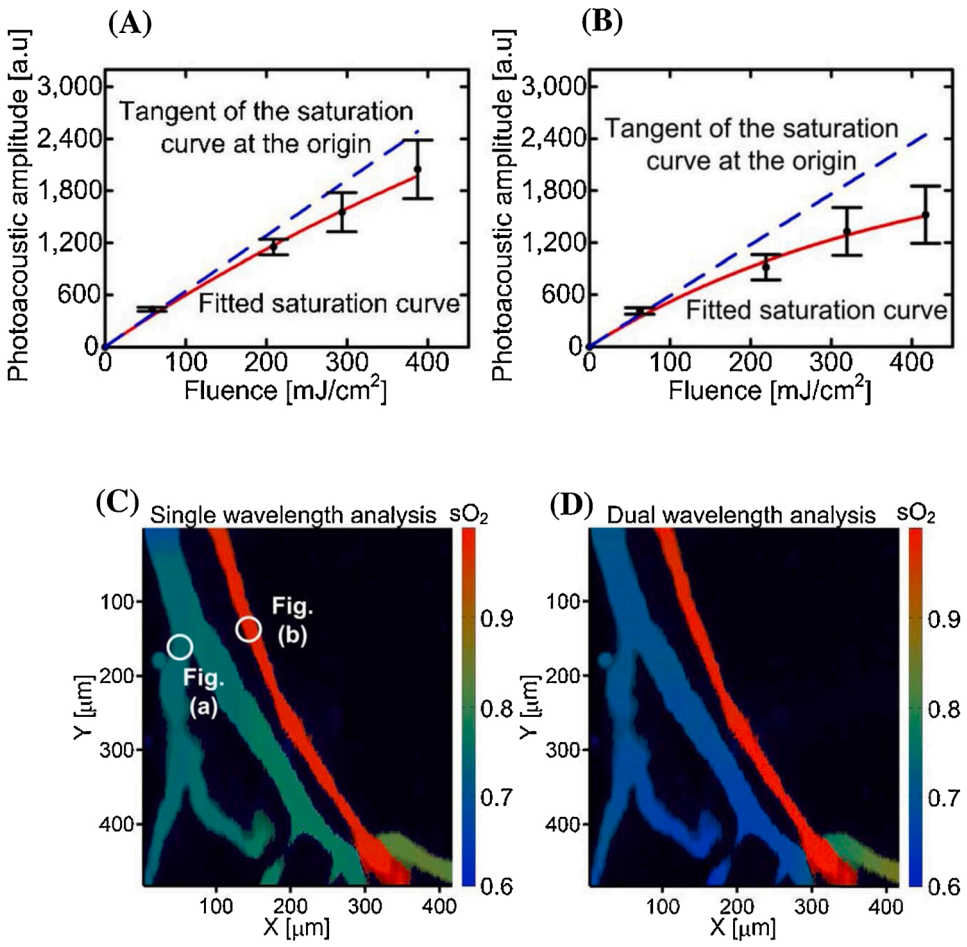

Fig. 3. PA signal as a function of the optical fluence at **(A)** low sO_2 location (vein) and **(B)** high sO_2 location (artery). sO_2 mapping measured using **(C)** single-wavelength and **(D)** dual-wavelength approaches. Figures reproduced with publisher's permission [24].

and the optical fluence is required, the nonlinear mechanism can be avoided by decreasing the optical fluence F or increasing the pulse duration τ_{laser} to ensure $I \ll I_{sat}$. To provide a quantitative example, HbO_2 and HbR do not saturate when irradiated with a 4 ns pulsed laser until F reaches 50 and 280 mJ/cm^2, respectively (Fig. 3A and B, respectively), which exceed the safety standard of MPE for nanosecond pulsed lasers (ANSI Z136.1-2014). This also suggests that using the same imaging system and optical intensity, absorbers with lower σ_{A0} and τ_{eff} (such as HbR) help avoid the saturation effect compared with those with higher σ_{A0} and τ_{eff} (such as HbO_2).

2.2. Thermal-based nonlinearity

2.2.1. Mechanism

The Grueneisen parameter Γ in Eq. (1) is given by

$$\Gamma = \frac{\beta c^2}{C_p}, \tag{7}$$

where β denotes the thermal expansion coefficient, c is the speed of sound, and c_p signifies the heat capacity. Among the three parameters (β, c, and c_p), the thermal expansion coefficient β exhibits the most notable dependence on temperature $\beta = \beta(T)$ [25–30] and needs to be taken into account when the temperature increase is significant. However, in most cases of PA imaging, the local temperature rise ΔT induced by pulse laser illuminations is often ignored by assuming that the thermodynamic parameters (β, c, and c_p) are constant, which no long holds true when ΔT is significant. As depicted in Fig. 1B, the PA amplitude increased considerably with a significant transient temperature rise ΔT, the reason of which is clarified as follows. Due to the fact that the temperature rise ΔT and thermal expansion are the cause and effect, *i.e.*, thermal expansion occurs after a temperature rise ΔT, the thermal expansion coefficient can be expressed as $\beta(T) = \beta(T_0 + \Delta T)$. Based on the Taylor series expansion, $\beta(T)$ is expressed as [30,81],

$$\beta(T) = \beta(T_0 + \Delta T) = \underbrace{\beta_0}_{\text{Linear term}} + \underbrace{\Delta T \frac{d\beta}{dT}|_{T=T_0}}_{\text{Nonlinear term}} \tag{8}$$

where β_0 is the expansion coefficient at the baseline temperature T_0. Higher-order derivative terms are neglected by assuming a proportional correlation between β and T, in which case $\frac{d^2\beta}{dT^2}|_{T=T_0} = 0$. The linear dependence of β on temperature is a commonly used approximation in photoacoustic imaging and is applicable for water-based and fatty tissues [82]. The expansion coefficient β of water as a function of temperature T is presented in Fig. 4A and discussed later in this section.

Eq. (8) reveals a linear term β_0 and nonlinear term $\Delta T \frac{d\beta}{dT}|_{T=T_0}$, which characterize the correlation between the PA signal and the local fluence F. To analyze the nonlinear term, the temperature rise ΔT is calculated using the thermodynamics law, $\Delta T = Q/\rho C_p$, where Q is the thermal energy for generating thermoelastic expansion in a target. Note that Q equals the product of the thermal energy arising from optical absorption Q_A ($= \eta_{th}\mu_a F$) and a proportionality factor $\gamma : Q = \gamma Q_A$. The factor γ accounts for the influence of thermal confinement on the thermal energy: $\gamma = 1$ when thermal confinement is satisfied (*i.e.*, no heat conduction occurs during the pulse duration); $\gamma < 1$ when unsatisfied thermal confinement takes place, which is because a fraction of total heat Q_A

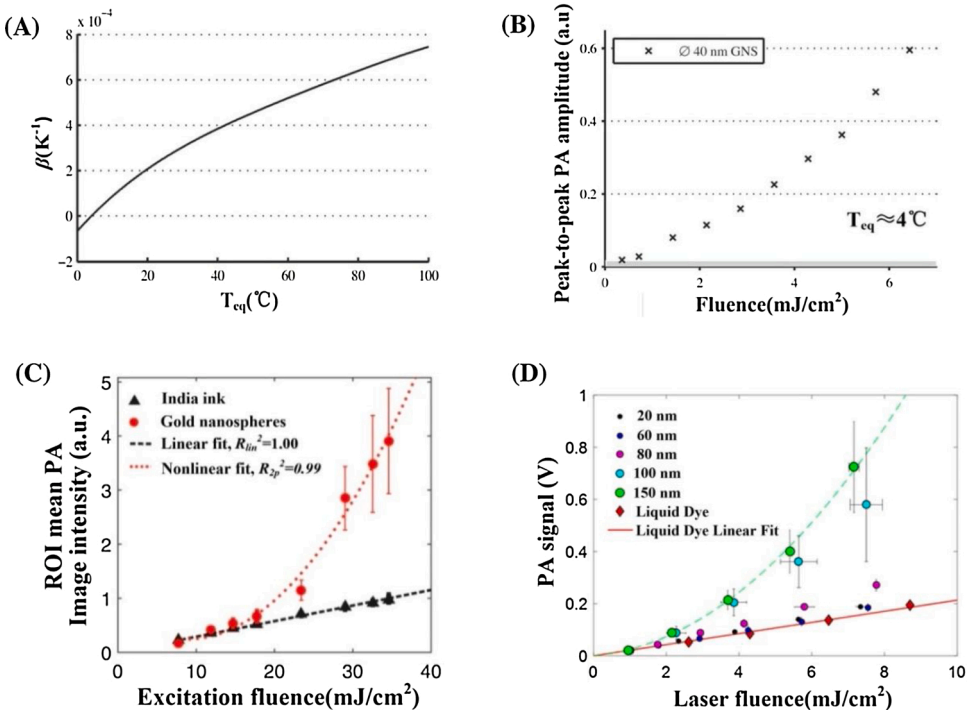

Fig. 4. Investigations of the mechanism of thermal-based nonlinearity. **(A)**Water expansion coefficient β as a function of temperature [30]**(B)** The PA signal vs. the optical fluence of gold nanosphere at approximately 4 °C [30]. **(C)** PA–F curves for both colloidal suspension of gold nanoparticles and diluted India ink [32]. **(D)** Experimental results of GNP diameter effect on thermal-based nonlinearity at room temperature [31]. Figures reproduced with publisher's permission [30–32].

transfers from the target to the surroundings, thus $Q < Q_A$. With the expression of $\Delta T = \gamma\eta_{th}\mu_a F/\rho C_p$, β can be expressed as,

$$\beta(T) = \beta_0 + \frac{\gamma\eta_{th}\mu_a F}{\rho C_p}\frac{d\beta}{dT|_{T=T_0}} \tag{9}$$

Consequently, the nonlinear term is fluence F dependent, which leads to a parabolic correlation between the PA signal and F (combining Eqs. (1), (7) and (9)) as follows:

$$PA = c_1 F + c_2 F^2, \tag{10}$$

where $c_1 = k\eta_{th}\mu_a c^2\beta_0/C_p$ and $c_2 = k\gamma\eta_{th}^2\mu_a^2 c^2\frac{d\beta}{dT|_{T=T_0}}/\rho C_p^2$. When ΔT is sufficiently small, based on Eq. (8) the nonlinear term is insignificant, in which case the linear dependence of the PA signal on the optical fluence is still applicable. However, in some cases, ΔT cannot be neglected and leads to a nonlinear dependence of PA on F, which will be discussed in the following sections.

2.2.2. *Influencing parameters*

According to Eq. (8), β_0 and ΔT are the two parameters affecting thermal-based nonlinearity. For water-rich soft biological tissues, when the temperature approaches 4 °C, water is at the critical point between thermal expansion and thermal contraction, indicating a zero expansion coefficient β_0, as depicted in Fig. 4A (data obtained from [83]). In this case, the nonlinear dependence shown in Eq. (8) becomes dominant as the linear dependence vanishes. Simandoux et al. [30] measured the PA–F curve of a gold nanosphere immersed in water ($T_0 \approx 4$ °C), the results of which demonstrate high nonlinear dependence on the optical fluence (Fig. 4B).

In cases of a significant temperature rise ΔT, the nonlinear dependence becomes evident even under conditions without temperature confinement ($T_0 = 4$ °C). Gold nanoparticles, in particular, have been demonstrated [27,28,31,32,81] to exhibit obvious thermal-based nonlinearity. This is mainly due to the large absorption cross-section σ_A caused by plasmon resonance, which induces a significant temperature rise during laser illumination. This is the main reason that gold nanoparticles (GNPs) are widely applied in photothermal therapy [84–86]. GNPs and India ink were employed in previous work [32] to depict a significant contrast between nonlinear (GNPs) and linear (India ink) fluence dependences (Fig. 4C). The results shown in both Fig. 4B and C indicate that strong nonlinear correlation occurred at low to modest laser fluence.

It is noteworthy that the thermal confinement may be violated when employing GNPs [27,81,87]. This is because the nanometer-scale size and high thermal conductivity of GNPs may result in the thermal relaxation time (τ_{th}) being smaller than the laser pulse duration (τ_{laser}). The equation to quantify τ_{th} is given in Section 2.4.1. The unsatisfied thermal confinement causes a portion of the detected PA amplitude arising from the surrounding media [81,87,88], *i.e.*, from water, if a GNP solution or suspension is used. This is due to the occurrence of the heat conduction between the GNPs and water within the time scale of τ_{laser}, which causes the thermal expansion of the surrounding water, thereby inducing the PA signal of the water media. As a result, the detected PA signal composes of the signals from both the GNPs and surrounding media [88,89], expressed as $PA_{total} = PA_g + PA_m$, where subscripts g and m indicate the GNPs and water media, respectively. It is worth mentioning that the existence of PA_m does not change the parabolic correlation between the detected PA signal (PA_{total}) and the optical fluence F (*i.e.*, $PA_{total} = c_1F + c_2F^2$). However, the coefficients c_1 and c_2 would be different than those in Eq. (10). The unchanged parabolic form with and without considering the contribution of PA_m to PA_{total} is because PA_m itself is a parabolic function of the optical fluence F, which will be elaborated as follows. The expansion coefficient of water media (β_m) can be expressed using Eq. (8), thus containing the influence of the optical fluence F due to the existence of the nonlinear term $\Delta T\frac{d\beta}{dT|_{T=T_0}}$. By substituting β_m back into the PA signal generated by water (PA_m) [88, 89], the first-order (F) and second-order (F^2) terms of the optical fluence appear in PA_m. Thus, as mentioned earlier, PA_m exhibits a parabolic form, providing that a significant transient temperature rise occurs upon the laser illumination. As a result, the detected PA signal for a GNP

solution/suspension (PA_{total}) demonstrates a parabolic dependence on the optical fluence F, because the sum of two parabolic functions (PA_g and PA_m) remains a parabolic one (PA_{total}). The above conclusions are based on the assumption that the expansion coefficients for both GNPs (β_g) and water media (β_m) can be estimated using Eq. (8).

In the case of GNPs, other factors may also affect the exhibition of thermal-based nonlinearity. For example, Pang et al. [31] experimentally investigated the effect of nanosphere size of GNPs on nonlinearity (Fig. 4D). The results indicate that at large GNP diameters (such as 100 and 150 nm), the GNP suspension exhibits a strong nonlinear behavior, whereas the suspension of GNPs with diameters less than 80 nm did not show obvious nonlinearity at room temperature, except when the nonlinearity was manifested through other mechanisms such as aggregation [28] or bubble formation [90]. This diameter effect (Fig. 4D) agrees with the results shown by Simandoux et al. [30], where the nonlinearity of GNPs with a diameter of 40 nm in aqueous solution was not detected at room temperature, although further studies are required to explain the physics of the diameter effect of GNPs on nonlinearity.

2.2.3. Applications

2.2.3.1. Discrimination between different absorbers. Thermal-based nonlinearity can be applied as a discrimination mechanism [30] between different absorbers. Nonlinear absorbers (*i.e.*, absorbers inducing high ΔT) and linear absorbers (*i.e.*, absorbers inducing low ΔT) exhibit different features in PA imaging. The differences are characterized by (1) the PA–F curve and (2) PA–temperature curve, respectively. In the PA–F curve, the two absorbing species, corresponding to the linear dependence (Eq. (1)) and nonlinear dependence (Eq. (10)) of the PA signal on the optical fluence F, display a linear vs. parabolic correlation, as illustrated in Fig. 5A. These different characteristics can be used to differentiate between the aforementioned two types of absorbing particles, instead of employing the conventional approach based on PA spectroscopy.

In addition to the PA–F curve, the PA–temperature curve demonstrates the potential to detect and identify different absorbers [30] as the nonlinear and linear absorbing species demonstrate different PA–temperature curve trends. In the PA–temperature curve, the temperature is the equilibrium temperature T_0 of the absorbers determined by the environment. For linear absorbers (*i.e.*, absorbers with low ΔT), according to Eq. (8) the expansion coefficient $\beta(T_0 + \Delta T) \approx \beta_0$. Hence, the PA– T_0 curve essentially reflects the $\beta_0 - T_0$ curve (Fig. 4A). This is because the remaining parameters in the expression of the PA signal (Eqs. (1) and (7)) can be considered as temperature insensitive compared with β_0, which shows a significant dependence on temperature. Although the speed of sound c is also affected by temperature, it has a secondary effect on the PA dependence on temperature because its sensitivity to temperature $c = c(T)$ is rather low compared with the expansion coefficient $\beta = \beta(T)$. Therefore, the tendency of PA vs. T_0 curve is determined by the $\beta_0 - T_0$ curve. The only difference between the two curves (PA– T_0 and $\beta_0 - T_0$) lies in the range of $T_0 < 4$ °C, where β_0 indicates negative values, whereas PA can only have positive values owing to the Hilbert transform applied in signal processing. Hence, the PA– T_0 curve for linear absorbers demonstrates a profile as shown in Fig. 5B (solid line), with two lines having an intersection at 4 °C. For nonlinear absorbers (*i.e.*, absorbers inducing high ΔT), the relation $\beta(T_0 + \Delta T) \approx \beta_0$ is not applicable as the nonlinear term $\Delta T \frac{d\beta}{dT}|_{T=T_0}$ in Eq. (8) needs to be accounted for. Owing to this nonlinear term, the $\beta - T_0$ curve is shifted up by $\Delta T \frac{d\beta}{dT}|_{T=T_0}$ compared with the $\beta_0 - T_0$ curve, as $\Delta T \frac{d\beta}{dT}|_{T=T_0}$ shows positive values throughout the entire temperature

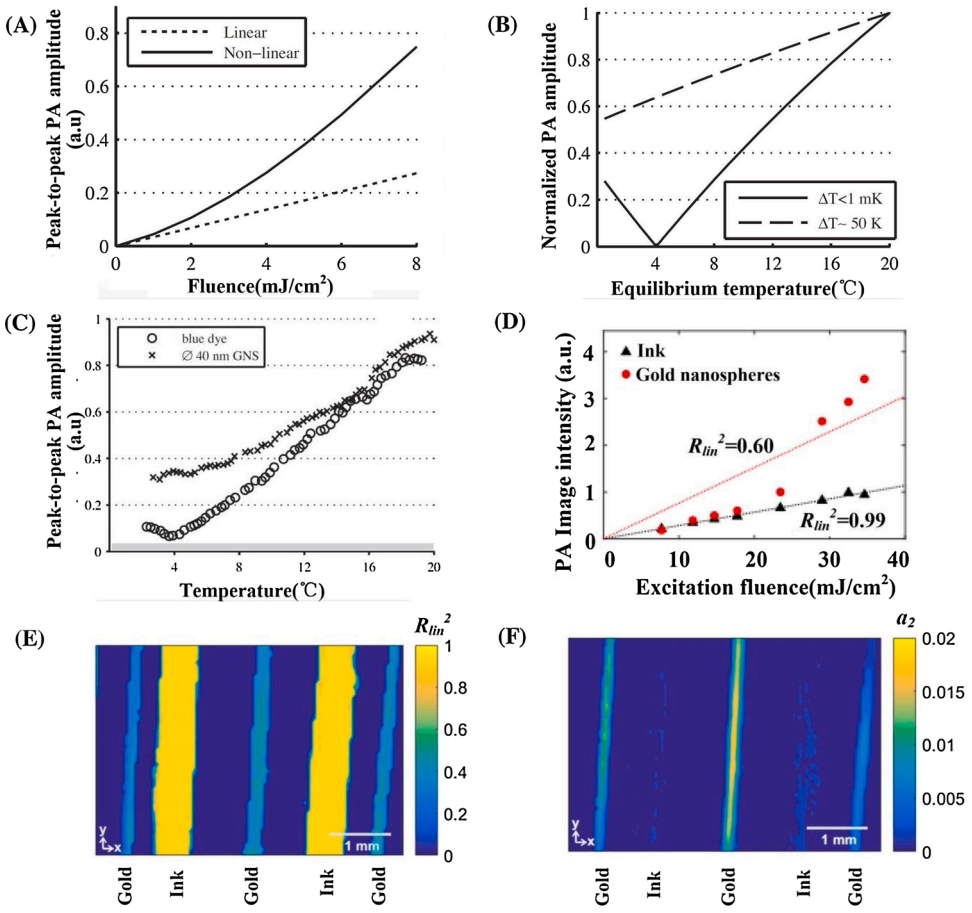

Fig. 5. Theoretical and experimental explorations in the application of thermal-based nonlinearity. **(A)** Theoretical results of PA signal as a function of temperature. Solid line: absorber with low ΔT. Dashed line: absorber with high ΔT. **(B)** Theoretical prediction linear and nonlinear PA–F curve at T_0=20 °C. **(C)** Experimental results of PA signal as a function of temperature. Circle: dye molecules. Cross: gold nanosphere. **(D)** Linear fit analysis for single voxel. R_{lin} for ink is considerably higher than R_{lin} for GNPs. Triangle: ink. Dot: gold nanosphere. **(E)** Plot of R_{lin} in an MAP image. **(F)** Plot of a_2 in an MAP image. Figures reproduced with publisher's permission [30,32].

range in Fig. 4A. For absorbers with significantly high ΔT, the nonlinear term $\Delta T\frac{d\beta}{dT|T=T_0}$ is sufficiently high such that the $\beta_0 - T_0$ curve is shifted above the x-axis. Without the negative values of β below 4 °C, the PA– T_0 curve for nonlinear absorbers presents a positive correlation with temperature (dashed line in Fig. 5B). The experimental results of dye molecules (linear absorber) and gold nanospheres (nonlinear absorber) in Fig. 5C both demonstrate consistency with the theoretical predictions (Fig. 5B). To summarize, these absorbers can be resolved by both the PA–temperature curve and PA–F curve. In other words, thermal-based nonlinearity offers an alternative way to discriminate different absorbers, without resorting to the conventional method such as PA spectral imaging [91–93].

Schrof et al. [32] extended the application to the selective detection of nonlinear absorbers (GNPs) from a strong absorbing background. The spatial distribution of different absorbers (India ink and GNPs) was discriminated based on their own characteristics of the PA–F curve. The ink-based absorbers exhibited a linear PA signal with respect to F, as follows:

$$PA = a_1 F \tag{11}$$

Meanwhile, the GNPs exhibited a parabolic function of the optical fluence,

$$PA = a_1 F + a_2 F^2 \tag{12}$$

Both Eqs. (11) and (12) were applied to PA–F curve fitting for two types of absorbers (India ink and GNPs). When using Eq. (11), the coefficient of determination in linear regression (R_{lin}) was employed to distinguish between linear absorbers (India ink) and nonlinear absorbers (GNPs), as GNPs showed a considerably lower R_{lin} value than India ink (R_{lin}≈1) in the linear fitting because of its nonlinear F dependence (see Fig. 5D). When Eq. (12) was applied for the fitting, the coefficient a_2 was used as an indicator to differentiate these two types of absorbers because a_2 equals zero theoretically for linear absorbers and shows a non-zero value for nonlinear absorbers (GNPs). Instead of using the amplitude of the PA signal, the two coefficients, namely R_{lin} and a_2, were plotted respectively to provide the spatial distribution image of both the GNPs and India ink, as illustrated in Fig. 5E and F.

This method was validated using a tissue phantom comprising five parallel tubes filled with either a colloidal suspension of GNPs or diluted India ink, as shown at the bottom of Fig. 5E and F. By plotting the R_{lin} value (Fig. 5E), the spatial pixels where the linear absorbers were located can be differentiated from the nonlinear absorbers based on their unique ranges of R_{lin}. By employing the value of a_2 (Fig. 5F), one can extract the spatial pixels that contain nonlinear absorbers and automatically eliminate unnecessary signals of other linear absorbing species from the background. To summarize, this method offers a single-wavelength approach to differentiate different absorbers and provide their spatial distributions by using the linear and nonlinear properties of their fluence dependences.

2.2.4. Occurrence conditions

Thermal-based nonlinearity arises from the dynamic transient change in the thermal expansion coefficient during pulsed illumination. The nonlinear contribution becomes significant if the temperature rise is sufficiently high to affect the value of $\beta(T)$ during illumination. To intensify this nonlinear mechanism, the weighting of the nonlinear term, which is determined by ΔT (Eq. (8)), can be increased using absorbing species with high absorption cross-sections, such as GNPs, which induce nonlinear effects even with low to modest laser fluences (Fig. 4B–D). Furthermore, the nonlinear effect can be amplified by making the coefficient of the linear term (β_0) zero. For example, for GNP suspensions where the PA signal is primarily from water, as described in Section 2.2.2, this can be realized by immersing the absorbing species into water at 4 °C. Similarly, these procedures can be adopted in reverse to avoid nonlinear correlations. Theoretically, thermal-based nonlinearity should occur in any absorber, providing a significant transient temperature ΔT is triggered during laser illumination. The significant ΔT changes the relative magnitude between the nonlinear and linear weights in PA signals (Eq. (8)), thereby manipulating the exhibition of the nonlinearity. In practice, ΔT is negligible for many absorbing species, which is the reason that the thermodynamic parameters (β, c, and c_p) are considered constant in most cases. Thus far, in addition to GNPs, few absorbing species have been reported to exhibit significant thermal-based nonlinearity. Thermal-based nonlinearity of the PA signal with respect to the optical fluence still needs thorough investigation in the future to demonstrate its application with more absorbing species.

2.3. Resolution-dependent nonlinearity

2.3.1. Mechanism

The depth-resolved optical fluence $F(z)$ inside an object is expressed as $F(z) = F_0 exp(-\mu_a z)$ [33,34] where F_0 denotes the optical fluence on the surface of the object, as depicted in Fig. 1C. Hence, the PA signal at any arbitrary depth z is expressed as

$$PA(z) = k\Gamma\eta_{th}\mu_a F_0 exp(-\mu_a z) \tag{13}$$

Theoretically, the PA signal on the surface ($z = 0$) of an object exhibits a linear correlation with the absorption coefficient μ_a because the exponential term $[exp(-\mu_a z)]$ vanishes in Eq. (13). However, in actual cases, owing to the limited axial resolution caused by the limited bandwidth of the ultrasound transducer, the PA technique cannot resolve targets infinitely fine. Consequently, the detected PA amplitude is an accumulation of the PA signals within an axial pixel Δz,

$$PA_{detected} = \int_0^{\Delta Z} PA(z)dz = k\Gamma\eta_{th}F_0[1 - exp(-\mu_a \Delta z)], \tag{14}$$

where Δz denotes the axial resolution of the PA system. Based on Eq. (14), the detected PA signal on the surface (z = 0) of an absorbing medium demonstrates a negative exponential correlation with μ_a [33–35], as shown in Fig. 1C. For a PA detection system with a sufficiently large transducer bandwidth and a low enough absorption coefficient, *i.e.*, both Δz and μ_a are approximately zero, and based on the Taylor series expansion, Eq. (14) can be approximated as

$$PA_{detected} = k\Gamma\eta_{th}F_0\mu_a\Delta z, \tag{15}$$

where the detected PA signal still remains a linear dependence on μ_a. However, when the conditions above are not satisfied, the linear correlation between PA and μ_a starts to lose its validity and a negative exponential dependence appears (Fig. 6A). This nonlinear effect is referred to as the absorption saturation effect in previous studies [33, 34]. In this paper, we refer to this mechanism as resolution-dependent nonlinearity to avoid confusion with the absorption-saturation induced by the optical fluence discussed in Section 2.1.

2.3.2. Influencing parameters

The axial resolution Δz and absorption coefficient μ_a are the two influencing parameters of resolution-dependent nonlinearity. The effect of these two parameters on the nonlinear dependence can be observed in Fig. 6A [34]. This nonlinear effect is evident when (1) the axial resolution is low (*i.e.*, Δz is high) or (2) the absorbing media has a strong μ_a.

To study the mechanisms of the two influencing parameters, theoretical studies were conducted [33] where the PA pressure rise was simulated as a function of axial depth under different values of μ_a (Fig. 6B). At the surface of the sample ($z = 0$), as shown in Fig. 6B, a higher μ_a resulted in a higher PA pressure rise according to Eq. (1). However, with increasing depths owing to the exponential decrease in F with the absorption coefficient ($F = F_0 exp(-\mu_a z)$), the PA pressure rise with higher μ_a decayed faster in depths than those with lower μ_a (Fig. 6B). This explains the detected PA amplitude, *i.e.*, the area enclosed by the PA pressure curve, horizontal axis, and vertical axis in Fig. 6B,

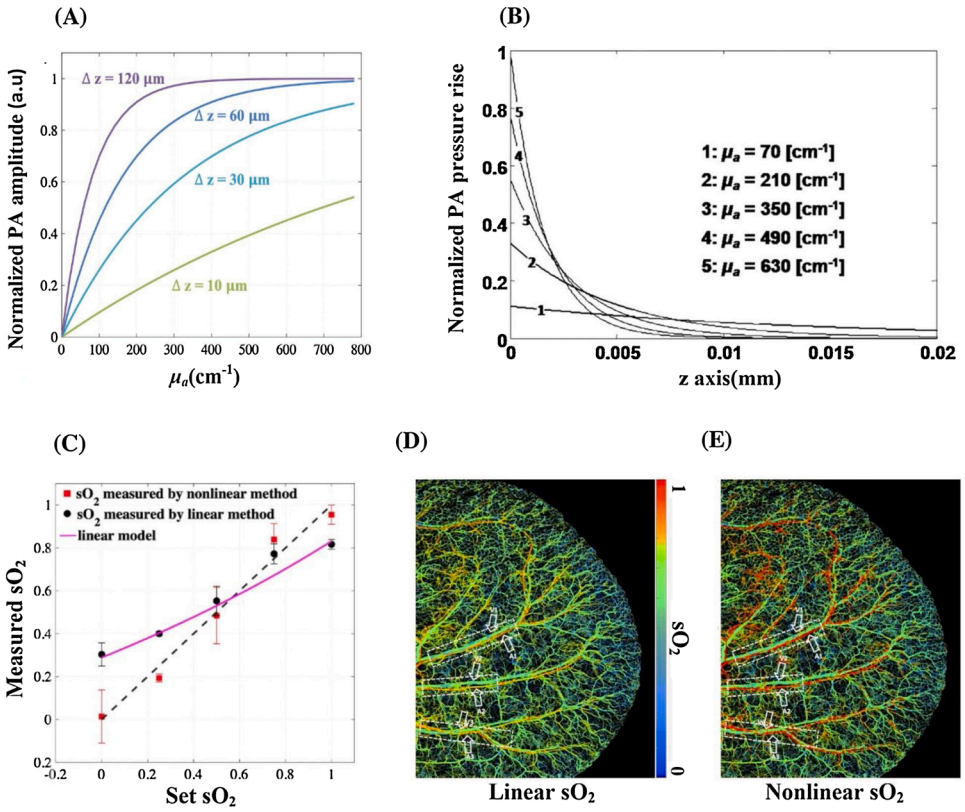

Fig. 6. Results of numerical simulations and experimental investigations of resolution-dependent nonlinearity. **(A)** $PA_{detected}$ as a function of absorption coefficient μ_a (Eq. (14)) under different axial resolutions Δz [34]. **(B)** PA pressure increase as a function of axial position z (Eq. (13)) under different absorption coefficients μ_a [33]. **(C)** sO_2 measurement of bovine blood using the nonlinear model [34] compared with the linear model. **(D)** *In vivo* nonlinear sO_2 imaging compared with the **(E)** linear model, demonstrated in a mouse ear. Figures reproduced with publisher's permission [33,34].

does not linearly reflect the increase in μ_a, particularly under high μ_a conditions. Meanwhile, if a higher axial resolution (shorter pixel element in z-axis) is applied, *e.g.*, 0.001 mm as shown in Fig. 6B, the nonlinear effect will not be obvious, as the space for the optical fluence to be attenuated with the depth is insufficient. In this case, the detected PA signal (*i.e.*, pixel-integrated PA value) mainly demonstrates a linear contribution because the PA signal on or near the sample surface ($z \approx 0$) linearly reflects absorption coefficient μ_a, and the attenuation of F at depths with μ_a is minimized. This justifies the fact that the detected PA signal maintains an approximately linear correlation with μ_a (Eq. (15)) when a sufficiently high axial resolution (low value of Δz) is applied. With knowledge regarding the influencing mechanism of the axial resolution Δz and absorption coefficient μ_a, the nonlinear mechanism can be avoided or strengthened by adjusting these two parameters. It is noteworthy that in extreme conditions (*e.g.*, $\Delta z > 120$ μm and $\mu_a > 300$ cm^{-1} as shown in Fig. 6A), the dependence of the PA signal on μ_a is completely removed, meaning that the PA amplitude is only affected by the optical fluence. This tendency is also reflected in Eq. (14) where the detected PA signal converges to $k\Gamma\eta_{th}F_0$ when μ_a or Δz is sufficiently high. The value of $k\Gamma\eta_{th}F_0$ indicates that the PA amplitude depends only on the optical fluence on the target surface F_0 when k, Γ and η_{th} are constants.

2.3.3. Applications

2.3.3.1. Compensating the resolution-dependent nonlinearity. When the resolution-dependent nonlinear effect is obvious, the conventional sO_2 measurement algorithm (Eq. (5)) is no longer applicable, as it is based on the linear dependence of the PA signal on μ_a and introduces systematic errors if applied in the nonlinear regime. Hence, a new method was developed [34] to compensate for the resolution-dependent nonlinearity. For the measurement of sO_2, the absorption coefficient is expressed as

$$\mu_a = rC_{HbT}(sO_2\varepsilon_{HbO_2} + (1 - sO_2)\varepsilon_{HbR}) \tag{16}$$

where r denotes a constant [94]; C_{HbT} is the concentration of the total hemoglobin; ε_{HbO_2} and ε_{HbR} are the molar absorption coefficients of HbO_2 and HbR, respectively. It is noteworthy that the molar absorption coefficient ε is proportional to the absorption cross-section σ, and $\varepsilon = N_a\sigma/1000\ln(10)$, where N_a is the Avogadro number. For a PA detection system with a finite axial resolution, the detected PA signal is obtained by combining Eqs. (14) and (16), expressed as follows:

$$PA_{detected} = k\Gamma\eta_{th}F_0[1 - exp(-rC_{HbT}\Delta z(sO_2\varepsilon_{HbO_2} + (1 - sO_2)\varepsilon_{HbO_2}))] \tag{17}$$

which comprises three unknowns, *i.e.*, sO_2 $k\Gamma\eta_{th}$, and $rC_{HbT}\Delta z$. By contrast, for the conventional approach of sO_2 measurement, two unknown variables (sO_2 and $k\Gamma\eta_{th}rC_{HbT}$) exist based on the PA amplitude expression $PA = k\Gamma\eta_{th}rC_{HbT}F_0(sO_2\varepsilon_{HbO_2} + (1 - sO_2)\varepsilon_{HbR})$, which is obtained by combining Eqs. (1) and (16). By comparing the above unknowns, it is clear that $k\Gamma\eta_{th}rC_{HbT}$ in the linear correlation has been disassembled into $k\Gamma\eta_{th}$ and $rC_{HbT}\Delta z$ in the nonlinear correlation, respectively, owing to the change in the mathematical structure of the expression of the PA signal in the nonlinear correlation (Eq. (14)) as opposed to the linear correlation (Eq. (1)). More specifically, in the linear correlation, μ_a is located at the same position as $k\Gamma\eta_{th}$ (Eq. (1)); hence, rC_{HbT} is also located therein based on the relationship between μ_a and rC_{HbT} (Eq. (16)). Therefore, only one term, $k\Gamma\eta_{th}rC_{HbT}$, is formed. However, in the nonlinear correlation, μ_a and rC_{HbT} remain in the exponential term ($exp(-\mu_a\Delta z)$); hence, $k\Gamma\eta_{th}$ and rC_{HbT} are separated, which consequently results in two unknown variables (*i.e.*, $k\Gamma\eta_{th}$ and $rC_{HbT}\Delta z$).

To quantify sO_2 when the resolution-dependent nonlinearity occurs, three wavelength measurements of PA signals were implemented [34] to solve Eq. (17). The effectiveness of this nonlinear model in sO_2 imaging was validated *via* phantom experiments on bovine blood (Fig. 6C) and in

the *in vivo* imaging of mouse ear (Fig. 6D and E), respectively. The former demonstrates that the nonlinear model provided consistent results with the set value of sO_2, and improved the sO_2 accuracy by up to 13 % compared with the linear method for fully oxygenated blood. The latter shows that the nonlinear sO_2 result agreed more closely with the physiological value compared with that obtained using the linear method.

2.3.4. Occurrence conditions

In contrast to the nonlinear mechanisms discussed in Sections 2.1 and 2.2, which characterize the correlation between the PA signal and the optical fluence F, the resolution-dependent nonlinearity depicts the dependence of the PA signal on the absorption coefficient μ_a. This nonlinearity exists provided that the PA detection system has a finite axial resolution. The nonlinearity becomes more prominent when imaging high-absorbing species using a transducer of low axial resolution (Fig. 6A). For biological tissue imaging, owing to the requirements of high imaging depth, the center frequency of the ultrasound transducer needs to be compromised because of the frequency-dependent acoustic attenuation. These are cases where resolution-dependent nonlinearity could occur and the nonlinearity compensation is necessary to be considered when the correlation between PA and μ_a is demanded, such as for functional PA imaging. Otherwise, attentions need to be taken when choosing the bandwidth of the ultrasound transducers in PA functional imaging.

In some cases, this nonlinear phenomenon is not obvious and can be approximated as a linear one. For example, when imaging a low absorbing target (*i.e.*, $\mu_a < 200\ \mathrm{cm}^{-1}$) with a high bandwidth transducer (*i.e.*, $\Delta f > 50$ MHz), which corresponds to an axial resolution $\Delta z < 27\ \mu\mathrm{m}$, according to Eq. (14) and Fig. 6A, the nonlinearity can be neglected and the PA signal demonstrates an approximate linear dependence on μ_a. Fig. 6A shows a quantitative analysis of Δz and μ_a values, where the linear dependence still remains valid.

2.4. Grueneisen-relaxation-based nonlinearity

2.4.1. Mechanism

There are two critical time scales involved in the generation of PA pressure rise: the thermal relaxation time (τ_{th}) and the stress relaxation time (τ_s) [19,20]. The former (τ_{th}) depicts the thermal diffusion of the voxel of interest upon being heated by a laser; it is given by $\tau_{th} = d_c^2/\alpha_{th}$, where d_c and α_{th} denote the heated region's characteristic dimension and the thermal diffusivity, respectively. The latter (τ_s) characterizes the pressure propagation in the voxel of interest and is expressed as $\tau_s = d_c/\mathrm{c}$, where c is the speed of sound. For instance, for a voxel of interest in soft tissue with a characteristic dimension $d_c = 30\ \mu\mathrm{m}$, the thermal relaxation time (τ_{th}) and stress relaxation time (τ_s) are estimated as 7 ms and 20 ns, respectively. As previously described in the Introduction section, the time duration of the excitation laser pulse (τ_{laser}) should be significantly smaller than both τ_{th} and τ_s for Eq. (1) to be applicable [19, 20]. It should be noted that the laser pulse interval employed in PA techniques usually exceeds the thermal relaxation time τ_{th}. Thus, the heat produced by the first laser pulse diffuses and is dissipated away before the second laser pulse excites the desired spot. This is the typical approach to ensuring independence (*i.e.*, neither PA signal affects the other) between different PA signals. However, if two identical laser pulses are applied sequentially within the absorbing target's thermal relaxation time (τ_{th}), the heat induced by the first laser pulse at the voxel of interest influences the amplitude of the second PA signal, owing to the increased Grueneisen parameter produced by the heat from the first laser excitation. This effect is referred to as the Grueneisen-relaxation (GR) effect and has been widely applied in PA techniques [36–41]. To further elucidate the GR effect, the PA signal generated by the first pulse is expressed as follows,

$$PA_1 = k\Gamma\eta_{th}\mu_a F \tag{18}$$

The second pulse induces a larger PA amplitude than the first due to the lack of sufficient time for the target to return to the baseline temperature, as illustrated in Fig. 1D. The second pulse is expressed as,

$$PA_2 = k(\Gamma + \Delta\Gamma)\eta_{th}\mu_a F \tag{19}$$

where $\Delta\Gamma$ denotes the change of the Grueneisen parameter in response to the change in local temperature ΔT caused by the first pulse. Generally, Γ is considered approximately proportional [82,95] to the local temperature because it is a function of the thermodynamic parameters (β, c, and c_p) shown in Eq. (7). $\Delta\Gamma$ can be expressed as [36,38],

$$\Delta\Gamma = b\eta_{th}\mu_a F \tag{20}$$

Eq. (20) is derived based on the approximately linear dependence of Γ on temperature ($\Delta\Gamma \propto \Delta T$) as discussed in Section 2.2.1. Given that the temperature rise ΔT is proportional to the total absorbed heat Q_A ($= \eta_{th}\mu_a F$), $\Delta\Gamma$ can be expressed by $b\eta_{th}\mu_a F$, where b is a constant that converts the thermal energy absorbed from the first pulse to the change of Grueneisen parameter [36, 38]. As a result, the Grueneisen-relaxation photoacoustic microscopy (GR-PAM) signal ΔPA is described as,

$$PA_{GR-PAM} = \Delta PA = PA_2 - PA_1 = kb{\eta_{th}}^2{\mu_a}^2F^2 \tag{21}$$

Consequently, a quadratic power dependence is established between the GR-PAM signal and the optical fluence F.

2.4.2. Applications

2.4.2.1. Improvement in imaging resolution. The GR effect can be used to improve lateral and axial resolutions in optical resolution photoacoustic microscopy (OR-PAM) [36–38]. These resolution-improvement capabilities have been demonstrated on tissue phantoms [36] and *in vivo* [38].

2.4.2.1.1. Lateral resolution. The lateral resolution ($R_{lateral}$) of OR-PAM depends on the full width at half maximum (FWHM) of the PA amplitude's spatial distribution. Assuming a Gaussian distribution of the optical fluence on the focal plane [36], we have

$$F(x,y) = \frac{E}{\pi w_0^2} exp\left(-\frac{x^2+y^2}{w_0^2}\right) \tag{22}$$

where E is the laser pulse energy, and w_0 denotes the Gaussian distribution waist on the focal plane for which the fluence amplitude is $1/e$ of its value at the beam center. In conventional OR-PAM, the PA amplitude on the focal plane is obtained by substituting Eq. (22) into Eq. (1), as,

$$PA(x,y) = k\Gamma\eta_{th}\mu_a F(x,y) = \frac{k\Gamma\eta_{th}\mu_a E}{\pi w_0^2} exp\left(-\frac{x^2+y^2}{w_0^2}\right) \tag{23}$$

where the FWHM is $2\sqrt{\ln 2}w_0$. Combining Eqs. (21) and (22), the PA signal for GR-PAM is given by,

$$PA_{GR-PAM}(x,y) = kb{\eta_{th}}^2{\mu_a}^2F^2(x,y) = \frac{kb{\eta_{th}}^2{\mu_a}^2E^2}{\pi^2 w_0^4} exp\left(-\frac{x^2+y^2}{w_0^2/2}\right) \tag{24}$$

The FWHM for GR-PAM is $\sqrt{2\ln 2}w_0$. Therefore, GR-PAM increases the $R_{lateral}$ of conventional OR-PAM by a ratio of $\sqrt{2}$ [36]. This improvement has been verified by imaging a sharp ink edge on a cover glass (Fig. 7A).

2.4.2.1.2. Axial resolution. PA techniques achieve a greater imaging depth than conventional optical microscopy, owing to the detection of time-resolved ultrasound waves. As a result, the axial resolution is defined acoustically and determined by the PA bandwidth Δf [1,96], that is, $R_{axial} = 0.88c/\Delta f$. This fundamentally differs from optical microscopy, where the axial resolution is determined by the optical focal zone. The PA signal along the z-axis in the optical focal zone (for a planar target with uniform μ_a) is an integration of the PA pressure rise in the lateral (x-y) plane: $PA(z) = \iint PA(x,y,z)dxdy$. Thus, for OR-PAM, $PA(z)$ is given by,

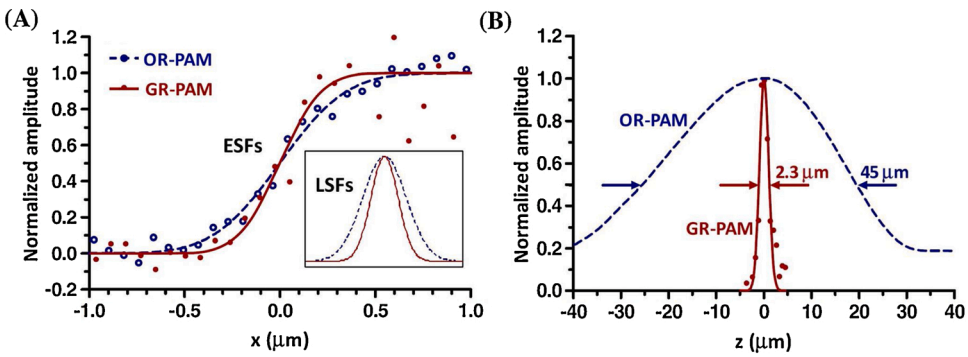

Fig. 7. Validation of the spatial resolution enhancement [36]. **(A)** Lateral resolution ($R_{lateral}$) measurements of OR-PAM and GR-PAM. The edge spread functions (ESFs) were obtained based on the PA amplitude across the sharp edge and the derivatives of ESFs give rise to the line spread functions (LSFs). The FWHM of ESFs for GR-PAM is smaller than OR-PAM by a factor of 1.6, which agrees with the theoretical value of $\sqrt{2}$. **(B)** Axial resolution was estimated for both GR-PAM and OR-PAM. R_{axial_GR} was assessed based on the FWHM of the fitted Gaussian curve of the differential PA signal (PA_{GR-PAM}) at different axial positions of a monolayer of RBCs. R_{axial_OR} was obtained from the FWHM of the A-line signal envelope (dashed line). R_{axial_GR} is measured to be 2.3 μm, which close to the theoretical prediction 2.4 μm ($1.8\lambda/NA^2$) and more than 18 times finer than R_{axial_OR}. Figures reproduced with publisher's permission [36].

$$PA(z) = \iint k\Gamma\eta_{th}\mu_a F(x,y,z)dxdy = k\Gamma\eta_{th}\mu_a E \tag{25}$$

When a planar target (*i.e.*, larger than $R_{lateral}$ in the x-y plane and infinitely thin in the z-direction) is placed at different depths of the focal zone, its axial PA signal $PA(z)$ does not change but remains a constant ($k\Gamma\eta_{th}\mu_a E$ (Eq. (25))) at different axial positions because the pulsed energy E does not vary between different axial positions. Thus, no FWHM exists within the focal zone, and optical sectioning is not possible [36–38]. However, in GR-PAM, the PA signal along the axial direction is given by,

$$PA_{GR-PAM}(z) = \iint kb\eta_{th}{}^2\mu_a{}^2F^2(x,y,z)dxdy \tag{26}$$

This is calculated by combining the definition of PA(z) with Eq. (21). The optical fluence distribution $F(x,y,z)$ on an arbitrary lateral plane at distance z from the focal plane is given by $F(x,y,z) = \frac{E}{\pi w^2(z)} exp\left(-\frac{x^2+y^2}{w^2(z)}\right)$, where w(z) is the Gaussian beam radius at distance z. After substituting the Gaussian distribution of $F(x,y,z)$ into Eq. (21) and performing several derivation steps, the GR-PAM signal becomes $PA_{GR-PAM}(z) = kb\eta_{th}{}^2\mu_a{}^2E^2/2\pi w^2(z)$. This suggests that when placing a planar target at different depths within the focal zone, the PA_{GR-PAM} signal becomes a function of the axial distance z, and the FWHM of the axial PA signal is determined to be $1.8\lambda/NA^2$, where λ and *NA* denote the optical wavelength and numerical aperture of the objective, respectively. The FWHM ($1.8\lambda/NA^2$) of the GR-PAM signal is two times the Rayleigh range, suggesting an optical axial resolution has been achieved [97,98], which is much higher than that of the conventional OR-PAM. The axial resolution enhancement has been verified by assessing the peak-to-peak PA amplitude of a monolayer of red blood cells (RBC) at different axial positions [36], as shown in Fig. 7B. Similar investigations into the optical sectioning capabilities of GR-PAM have also been reported in the literature [37,38].

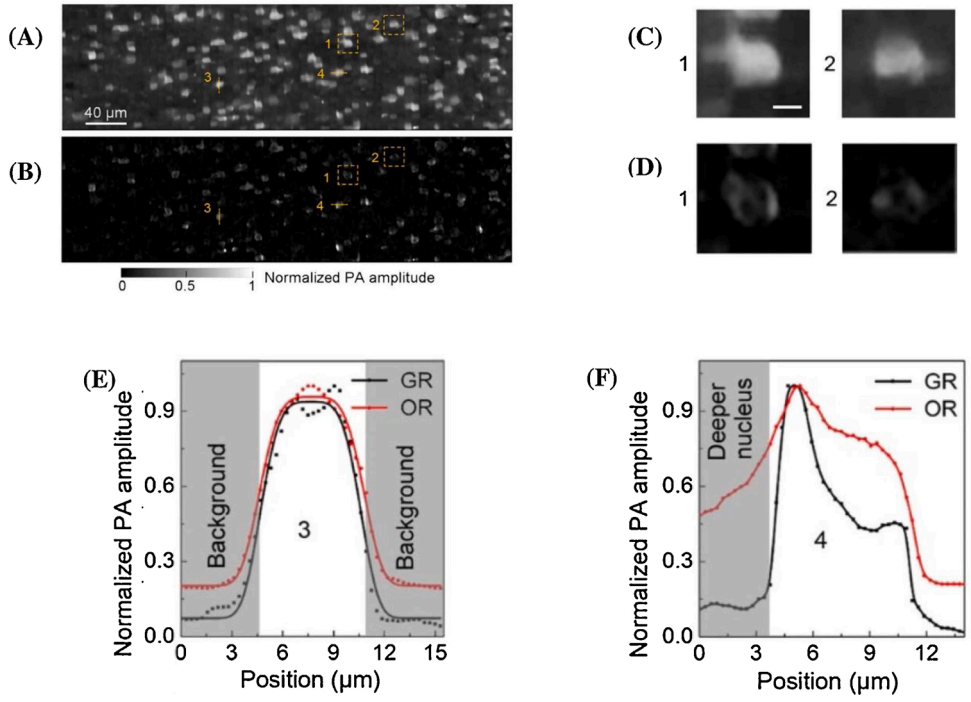

Fig. 8. Validation of the imaging contrast enhancement [37]. **(A, B)** A mouse brain slice imaged using OR-PAM and GR-PAM, respectively. **(C, D)** The magnifications of the square regions marked as 1 and 2 in **(A)** and **(B)**, respectively; here, the internal structures of the cell nuclei are unclear in OR-PAM **(C)** but resolved in GR-PAM **(D)**. **(E, F)** A-line profiles of the dot-cross sections marked as 3 and 4 in **(A)** and **(B)**, respectively. Figures reproduced with publisher's permission [37].

2.4.2.2. Imaging contrast improvement. Apart from the improvement of spatial resolution, the GR effect can also be used to enhance the imaging contrast [37]; this has been verified using ultraviolet laser illumination in both conventional OR-PAM and GR-PAM imaging of a mouse brain slice (Fig. 8A and B). The internal structure of the cell nuclei was unclear in OR-PAM (Fig. 8C) but resolved in GR-PAM (Fig. 8D). The quantitative imaging contrast comparison between the two aforementioned approaches proves that the imaging contrast was enhanced by a factor of 3.3, according to the line profile (Fig. 8E). This differs from the improvement in lateral resolution, which is characterized by a sharpening of the FWHM of the lateral PA signal profile. As shown in Eq. (21), the PA signal in GR-PAM exhibits a quadratic power dependence not only on (1) the optical fluence F but also (2) the absorption coefficient μ_a. Thus, the increase in image contrast achieved using GR-PAM arises from both quadratic dependences. In contrast, the lateral resolution improvement arises solely from the quadratic power dependence of the PA signal on the optical fluence. Of the two quadratic power dependences, the former produces a higher PA signal contrast between targets within the optical focal zone and out-of-focus targets, compared with linear OR-PAM. Meanwhile, the quadratic power of the absorption coefficient ($\mu_a{}^2$) further enables the absorbers with high absorption to exhibit even higher PA amplitudes, while the background (with low absorption) exhibits significantly lower PA signals. The contrast between them is governed by a quadratic power law ($\mu_a{}^2$), in contrast to the conventional linear OR-PAM, where the image contrast is determined solely by the first power of the absorption difference (μ_a). Unlike the quadratic power dependence on F (through which the image contrast enhancement relies on the relative positions between targets and the optical focal zone), the image contrast increase produced by the quadratic power dependence on μ_a is not position-dependent but species-specific. In other words, the contribution of $\mu_a{}^2$ to the image contrast increase is solely determined by the difference in absorbance coefficients between different absorbers, regardless of their locations.

2.4.2.3. Suppressing the side-lobe artifacts. Compared to a focused Gaussian beam, a Bessel beam substantially extends the focal depth [99] (Fig. 9A), which facilitates a consistent lateral resolution in the axial direction of OR-PAM. This avoids the tradeoff between the imaging resolution and the focal depth [40]. However, Bessel beams are known to suffer from side-lobe artifacts, as shown in Fig. 9A (the second row). This limits the application of Bessel beams in PA imaging as they introduce ghost signals due to the strong side-lobes. The GR effect, interestingly, shows potentials to resolve this problem by utilizing the nonlinear dependence on the optical fluence F to suppress the side-lobe artifacts [40] (Fig. 9B). To be more specific, the optical intensity I of a Bessel beam, as depicted by Fig. 9A (second column), is given by $I(r,z) = I_0(z)J_0{}^2(2.4048r/r_0)$, where $I_0(z)$ is the optical density at axial coordinate z, r is the transverse radial coordinate, J_0 is the zero-order Bessel function of the first kind, and r_0 signifies the radius of the central lobe. The above expression shows that the point spread function (PSF) of linear PA signals on the lateral plane is proportional to $J_0{}^2$. In such cases, the linear PA imaging still exhibits many side lobes, as shown in Fig. 9B (PA_1 and PA_2). However, when applying the GR effect, according to Eq. (21), the PSF of PA signals becomes the square of the Bessel beam profile, *i.e.*, the fourth power of J_0 ($J_0{}^4$). Since the amplitude of the central lobe is much higher than the side-lobes (Fig. 9A, second column), the ascending power dependence on J_0 enhances the amplitude of the central lobe to a much higher value and decreases the side-lobes to lower ones. This greatly enlarges the gap of amplitude between central and side lobes. As a result, the side-lobe artifacts in PA imaging are effectively suppressed by using the GR effect, as demonstrated by the image of nonlinear results (ΔPA) in Fig. 9B. This substantially broadens the application of Bessel beams in PA imaging.

2.4.2.4. Temperature measurement. The GR effect has been employed to quantify temperature distributions in deep tissues [39]. Instead of sequentially delivering two laser pulses, a burst of laser pulses ($N \geq 2$) is delivered to the target tissue within the time scale τ_{th}. This arrangement is presumably to assure a measurable difference in PA signal between the first and N-th pulses, based on the cumulative thermal effect of a number of consecutive laser pulses. The pressure rise induced by the N-th pulse is expressed as [100],

$$p_N = (\Gamma_0 + \Delta\Gamma)\eta_{th}\mu_a F = (\Gamma_0 + b\eta_{th}\mu_a F(N-1))\eta_{th}\mu_a F \tag{27}$$

where b denotes the first-order derivative of the Grueneisen parameter with respect to the absorbed photon energy, which is a constant value and has been reported in a previous work [100]. Expressing the first PA pressure rise as $p_1 = \Gamma_0\eta_{th}\mu_a F$ and combining it with Eq. (27), we obtain,

$$\frac{p_N - p_1}{{p_1}^2} = \frac{b}{{\Gamma_0}^2}(N-1) \tag{28}$$

Thus, Γ_0 can be directly determined using p_N and p_1. The pressure rises (p_N and p_1) are quantified from the detected PA signals (PA_N and PA_1), by calibrating the ultrasound detection system using the approach discussed in the literature [101]. As a result, the temperature is obtained according to the correlation between T and Γ in soft tissue [102],

$$T_0 = 115.89\Gamma_0 - 13.14 \tag{29}$$

Combining Eqs. (28) and (29) allows the absolute temperature in the tissue to be determined, as opposed to conventional PA thermometry [82,95,103–105], which offers relative temperature monitoring.

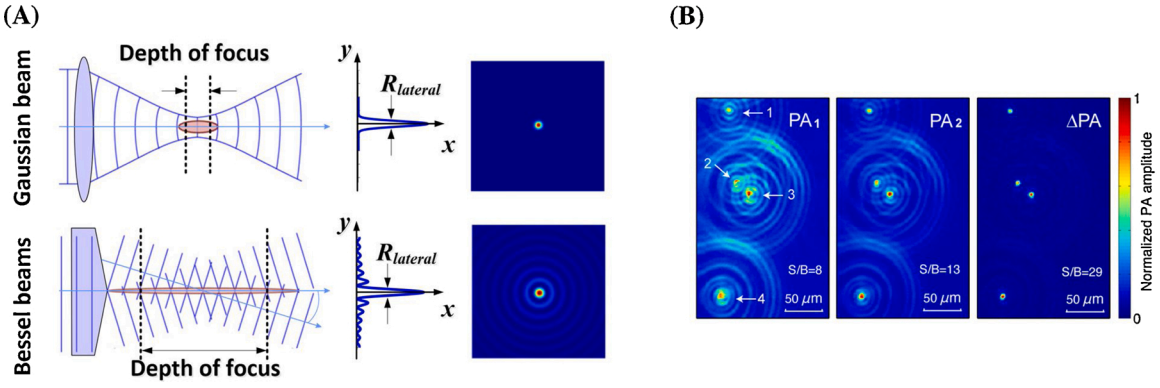

Fig. 9. The application of GR-based nonlinearity in suppressing the side-lobe artifacts of Bessel beams. **(A)** The Gaussian beam (first line) vs the Bessel beam (second line) [99]. The Bessel beam provides a much longer focal depth than the Gaussian beam but introduces side lobes. **(B)** The MAP images of single-layer red blood cell using a Bessel beam [40] as the excitation beam source. PA_1: linear results when no heating was applied. PA_2: linear results after the heating laser shot. ΔPA: nonlinear results (PA_2-PA_1). Figures reproduced with publisher's permission [40,99].

Therefore, this new approach eliminates the requirement that the baseline temperature be known *a priori*. Furthermore, when determining the absolute temperature, the conventional approaches assume that the changes in PA amplitude only arise through changes in temperature. This either (1) assumes that the tissue maintains its optical and acoustic properties over a large temperature range or (2) must pre-calibrate the variations of PA signal caused by tissue property changes before completely attributing the PA signal changes to temperature alterations. Interestingly, the new GR-effect-based approach offers a calibration-free measurement of absolute temperature, without employing the aforementioned assumption. The validity of this method has been confirmed by the temperature measurement of ink-filled tubes in tissue phantom at a 1.5-cm depth (Fig. 10A), and a good agreement between the measured and preset values was achieved (Fig. 10B). Measurements were further performed in mice at 2-mm depths, to demonstrate the feasibility of the method for *in vivo* temperature mapping [39].

The calibration-free PA thermometers can potentially facilitate the PA-guided therapies and temperature monitoring in some applications [106,107], such as the high-intensity focused ultrasound therapy and photothermal therapy. Combined with the PA-guided temperature regulation [107], further studies using the nonlinear approach are required to expand the PA thermometers towards *in vivo* application.

2.4.2.5. Preservation of heating memory. In the GR effect, as shown in Eq. (21), the PA signal not only reflects the properties of the second pulse but also contains information about the previous heating stage (*i.e.*, the optical fluence F employed for heating, and the optical absorption coefficient μ_a). Preserving the heating memory facilitates the extraction and utilization of previous heating information [108,109] and allows the two consecutive heating stages to be combined for better imaging quality [110].

2.4.2.5.1. Spectroscopy imaging. Instead of using a multi-wavelength pulsed laser, PA spectroscopy imaging adopts multiple continuous wave (CW) laser sources [each with a different wavelength (λ_i)], as well as a single-wavelength pulsed laser (λ_0) [108,109]. The imaging target was first heated by the CW laser before the second pulsed laser was applied to induce PA signals, as shown in Fig. 11A. The corresponding PA signals (with and without CW laser heating) are illustrated in Fig. 11B. The normalized difference between the two PA signals is obtained from Eqs. (18) and (19); it is expressed as,

$$(PA_1 - PA_2)\Big/PA_1 = \Delta\Gamma\Big/\Gamma_0 \propto \underbrace{\mu_a(\lambda_i)F_{cw}}_{\text{Heating properties (induced by CW laser)}} \tag{30}$$

where $\mu_a(\lambda_i)$ and F_{cw} denote the absorption coefficient at wavelength λ_i and the optical fluence of the CW laser, respectively. The ratio $(PA_1 - PA_2)/PA_1$ eliminates the influence of the pulsed laser ($\mu_a(\lambda_0)$, F_{pulse}) and retains only the heating properties ($\mu_a(\lambda_i)$, F_{cw}) induced by the CW laser. As a result, PA spectroscopy is achieved using the heating memory of the CW laser at specific wavelengths. This novel strategy has been validated by comparing its absorption spectroscopy results with those obtained using a spectrometer; a good agreement was achieved. The merit of this method lies in its low cost compared to conventional PA spectroscopy approaches, which use high-power multi-wavelength optical parametric oscillator (OPO) pulsed lasers [111,112], which are bulky and expensive.

The pulse duration of the CW laser in this study [108] exceeded the thermal relaxation time τ_{th} of the absorbing target, thus, thermal confinement was not satisfied by the CW laser during PA imaging. The unsatisfied thermal confinement indicates that thermal diffusion and heat deposition occur concurrently within the long duration of CW illumination, which is accounted for when determining the PA amplitude [108]. The failure to satisfy the thermal confinement conditions does not influence the validity of the correlation $\Delta\Gamma \propto \mu_a(\lambda_i)F_{cw}$ shown in Eq. (30). A more detailed mathematical illustration is presented in the supplementary materials of a previous work [100].

2.4.2.5.2. Combining merits of two distant spectra. At least two laser pulses are required for the GR effect; hence, this effect can exploit the advantages of the two spectra when using one pulse from each spectrum. For example, the mid-infrared (MIR) spectrum, which offers rich molecular information of biological samples, was combined with ultraviolet (UV) imaging, which enables high spatial resolution [110]. This was achieved by using a pulsed MIR laser to thermally tag the target and a pulsed UV laser to image it, as illustrated in Fig. 11C and D. The time lag between the two pulses satisfied the thermal confinement requirements. The UV pulse that detected the temperature rise, expressed as $PA_{UV2} = k(\Gamma + \Delta\Gamma)\eta_{th}\mu_{uv}(\lambda)F_{uv}$, was compared with an initial UV pulse without any thermal tag, expressed as $PA_{UV1} = k\Gamma\eta_{th}\mu_{uv}(\lambda)F_{uv}$. The increase in the Grueneisen parameter $\Delta\Gamma$ is a result of MIR thermal heating, $\Delta\Gamma = b\eta_{th}\mu_{MIR}(\lambda_i)F_{MIR}$. This method is referred to as ultraviolet-localized MIR photoacoustic microscopy (ULM-PAM). The difference between the two pulses is given by,

$$\Delta PA = PA_2 - PA_1 = kb\eta_{th}^2 \underbrace{\frac{\mu_{MIR}(\lambda_i)\mu_{uv}(\lambda)}{\text{Water background suppression}}}\underbrace{\frac{F_{MIR}F_{uv}}{\text{Resolution increase}}} \tag{31}$$

Equation (31) has two implications. On the one hand, the lateral resolution of ULM-PAM is governed by the term $F_{MIR}F_{uv}$. The product of the two Gaussian profiles of the optical fluence, with their expressions given by Eq. (22), leads to a smaller Gaussian beam radius $w(z)$ than either of the two profiles. In other words, the lateral resolution of ULM-PAM is higher than that of either MIR-PAM or UV-PAM. Given that the lateral resolution of MIR-PAM is considerably lower than that of UV-PAM, the combined results of $F_{MIR}F_{uv}$ are approximately equivalent to

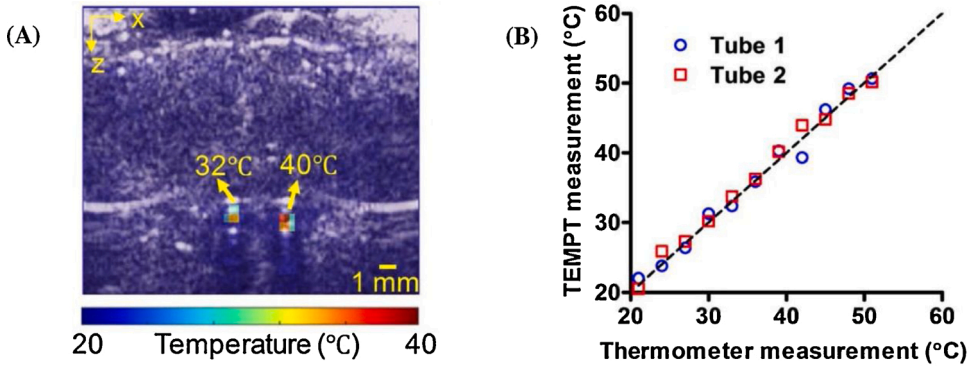

Fig. 10. Results of temperature measurements. **(A)** Representative temperature map of two tubes (shown in color) overlaid onto an ultrasound image (shown in gray). **(B)** The linear correlation between the measured temperatures and preset values, used to evaluate the accuracy of the proposed measurement approach. Figures reproduced with publisher's permission [39].

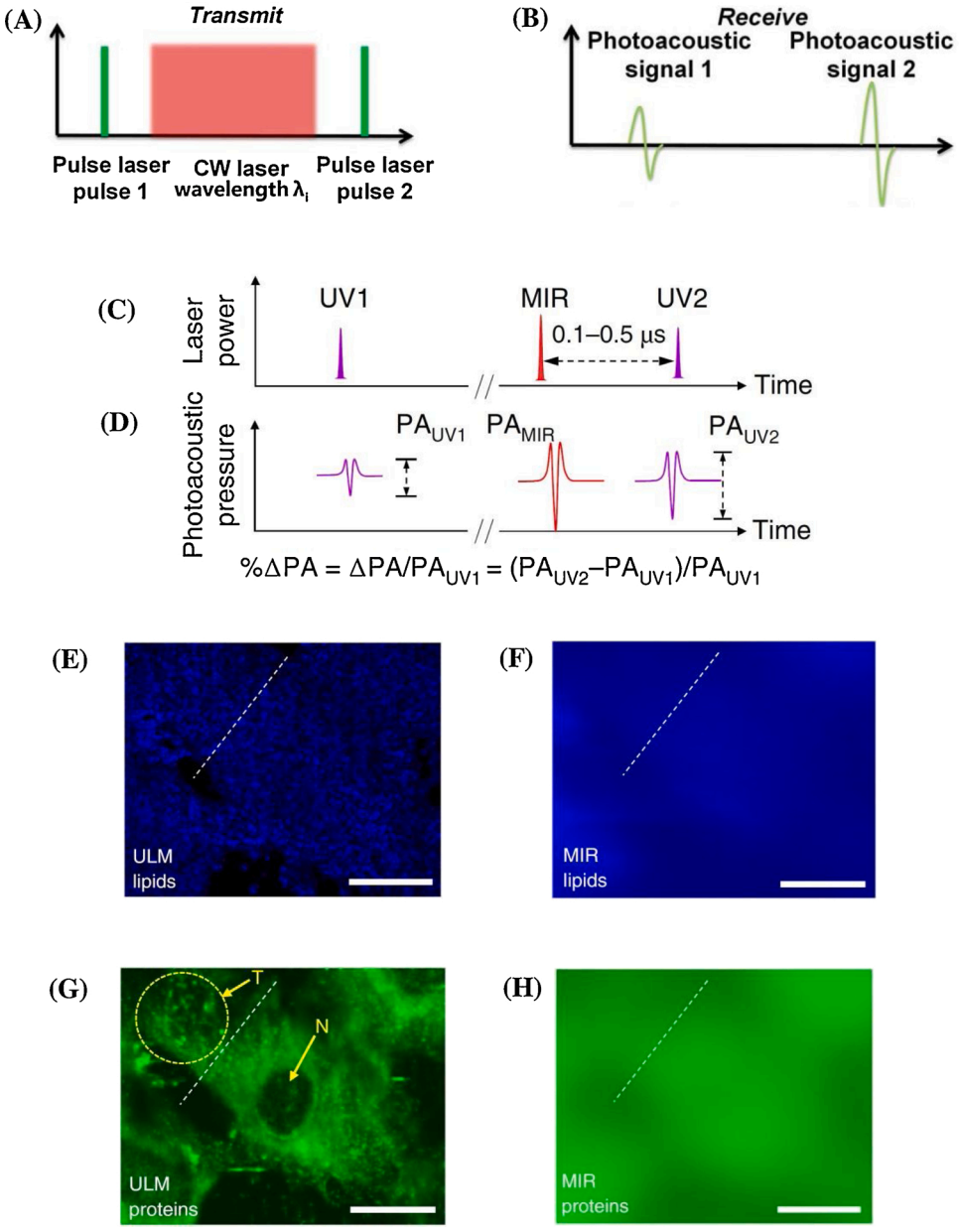

Fig. 11. Principles and results of the preservation of heating memory. **(A)** Pulse sequence pattern, including two pulsed laser excitations and one CW excitation for each measurement [108]. The wavelength of the CW laser is denoted as λ_i, where the subscript i denotes the different wavelengths applied to the heating process. **(B)**PA signals before and after CW laser heating [108]. **(C)** Principle of ULM-PAM, including two UV pulses and an MIR pulse [110]. **(D)** The corresponding PA signals of three pulses in ULM-PAM [110]. Lipid images produced using **(E)** ULM-PAM and **(F)** MIR-PAM. Protein images produced using **(G)** ULM-PAM and **(H)** MIR-PAM. Figures reproduced with publisher's permission [108,110].

the ultraviolet resolution. On the other hand, Equation (31) indicates that ULM-PAM combines the absorption contrasts of both MIR and UV, as reflected by the term $\mu_{MIR}(\lambda_i)\mu_{uv}(\lambda)$. Thus, the strong water background of the MIR wavelength is suppressed using this method, due to the low UV absorption of water. As a result, the water-background-suppressed MIR imaging of biological tissues (*e.g.*, lipids and proteins in cultured cells) are achieved at UV resolutions, as shown in Fig. 11 (E–H); this is one order of magnitude finer than the MIR resolution.

2.4.2.6. Summary. The aforementioned applications are chosen as the representative examples for the GR effect. Apart from the above-mentioned scenarios, the GR effect has also been employed in other fields. For example, owing to the ascending power dependence on the optical fluence, the GR effect was applied in wavefront shaping to achieve a diffraction-limited optical focusing in an optical scattering medium [41]. Furthermore, GR-based nonlinearity also shows potentials for tissue differentiation [113]. This is realized by extracting the term containing tissue-dependent properties (Γ, η_{th} and μ_a) using the nonlinear model. A similar work using the nonlinear mechanism to distinguish different types of materials was shown in Ref [114]. In this work, dual imaging contrast—both the optical absorption contrast (μ_a) and thermal contrast (τ_{th}) were employed independently to resolve different samples (muscles and fat tissues). Apart from the discrimination of targets, the nonlinear effect can also be applied to suppress a strong background when imaging magnetic nanoparticles [115], and even provide nanoparticle design guidelines [116,117]. These guidelines facilitate the synthesis and development of PA nanoamplifiers to realize nonlinear signal amplification and high imaging contrast. It is also worth noting that the technical aspects and variables of GR-PAM have been examined in Ref [118], including the wavelength selection, the laser fluence, the time delay and the relaxation function. These investigations were conducted to help achieve the highest nonlinear effect by optimizing both the heating and the probing efficiencies. The results of this work provide guidance for future developments of GR-based nonlinearity.

2.4.3. Occurrence conditions

In contrast to other aforementioned nonlinear mechanisms, which

are based on the nonlinearity of one measured PA signal, GR-based nonlinearity requires a double-excitation process to establish nonlinear dependence. Theoretically, this can be applied to any scenario provided the two laser pulses can be delivered within τ_{th} (for conventional OR-PAM in which the lateral resolution is 4 μm, τ_{th} is estimated as 0.1 ms for soft tissues). In practice, the subtracted signal ΔPA between the two pulses needs to be detectable (*i.e.*, above the noise level of a transducer) for GR-based nonlinearity to apply. A low SNR can occur for deep tissues *in vivo*, because the temperature increase induced by the first pulse may not be sufficient, owing to the strong optical scattering. However, a number of consecutive laser pulses ($N \geq 2$) [39] released within the time scale of τ_{th} may help address this problem. Compared with the aforementioned nonlinear mechanisms, this GR-based nonlinearity can be also completely avoided by not applying the two consecutive pulse delivery procedures. This feature, combined with the label-free mechanism, is the intrinsic advantage of GR-based nonlinearity over the other nonlinear mechanisms discussed above.

2.5. Reversible-switching-based and photobleaching-based nonlinearity

2.5.1. Mechanism

2.5.1.1. Reversible-switching-based nonlinearity. Reversibly switchable photoacoustic microscopy (RS-PAM) inherently exploits the photoconvertible properties of genetic reporter proteins, which allow absorption peaks to be red-shifted in a reversible fashion. More specifically, the 780 nm laser illumination red-shifts the absorption peak of proteins from the near-infrared to the red light-absorption state, decreasing the absorption coefficient at 780 nm. In contrast, the 630 nm wavelength allows the absorption peak to be shifted back to the near-infrared state, increasing the μ_a of proteins at 780 nm back to their original values. This allows for repeated testing in PA imaging. The states before and after 780 nm illumination are denoted as ON and OFF states, respectively [42]. Differential imaging between the two states (before and after 780 nm illumination) facilitates the removal of background noises, increases the image contrast, and enhances the resolution [42,119,120]. The PA signal of RS-PAM is represented as the difference between the two states [42]:

$$PA_{RS-PAM} = PA_{before} - PA_{after} \tag{32}$$

PA_{before} in Eq. (32) corresponds to the ON-state and reflects the original profile of the absorption coefficient μ_a before the photoswitching process. For simplicity, μ_a is considered uniformly distributed within the excitation spot (Fig. 1E.1), which is the approximation used for OR-PAM when the focal spot is sufficiently small. However, after laser illumination at 780 nm, the number of ON-state molecules (N_0) decreases because of the switching-off process; thus, a fraction of the protein molecules transit to the OFF state. This switching-off procedure is a stochastic process in which only a fraction of protein molecules are switched off during the single-pulse 780 nm illumination. The number of protein molecules switched off depends on the laser intensity. As a result, the absorption coefficient μ_a is no longer uniformly distributed but instead have a reduction profile $\mu_a(x,y)$ in the focal spot (Fig. 1E.2). This reduction profile $\mu_a(x,y)$ depends on the intensity profile $I(x,y)$ and therefore on the fluence profile $F(x,y)$. Differentiating between the two states permits the extraction of the absolute reduction profile $\mu_a(x,y)$ (*i.e.*, Fig. 1E.3). Consequently, the PA signal of RS-PAM not only reflects the excitation fluence distribution $F(x,y)$ but also the absorption coefficient profile $\mu_a(x,y)$, which directly depends on $F(x,y)$. This means PA_{RS-PAM} is not proportional to the optical fluence F but to its power. Using Eq. (32) and applying several approximations, the PA signal of RS-PAM is calculated as [42],

$$PA_{RS-PAM} \propto \Gamma \eta_{th} N_0 I^{bm+1} \propto \Gamma \eta_{th} N_0 F^{bm+1} \tag{33}$$

Eq. (33) establishes a nonlinear mechanism: a $bm+1$ degree power dependence of the PA signal on the optical fluence F, where b denotes the power dependence of the switching-off rate on the excitation intensity, and m signifies the order of the polynomial fitting to the signal decay. According to Eq. (33), a higher photoswitching rate b produces a higher-order PA signal power dependence on the optical fluence. In other words, the nonlinearity is more pronounced for faster photoswitching proteins. This nonlinear effect is referred to as reversible switching (RS) nonlinearity in this review.

2.5.1.2. Photobleaching-based nonlinearity. The principle of photobleaching-based (PB) nonlinearity [43] is analogous to that of RS nonlinearity; for instance, it similarly applies a double-excitation process, shown as,

$$PA_{PB-PAM} = PA_{i-1} - PA_i \propto \Gamma \eta_{th} N_0 I^{b+1} \propto \Gamma \eta_{th} N_0 F^{b+1} \tag{34}$$

where PA_{i-1} and PA_i denote two consecutive PA pulses. Similar to the RS effect, for simplicity, the absorbance coefficient μ_a before photobleaching is assumed to be uniformly distributed within the optical focal spot, as depicted in Fig. 1E.1. However, under laser excitations, the absorbers inside the focal spot become inhomogeneously bleached because of the Gaussian-distributed optical profile $F(x,y)$. This reduces the absorption profile $\mu_a(x,y)$ (Fig. 1E.2) inside the focal spot, with the reduction depending on $F(x,y)$. As a result, the differential in Eq. (34), which is equivalent to Eq. (33), reflects not only the optical fluence profile $F(x,y)$ but also the absorption distribution $\mu_a(x,y)$ produced by $F(x,y)$, as shown in Fig. 1E.3. Consequently, a $b+1$ degree power dependence between the PB-PAM signal and the optical fluence F is established, as depicted in Eq. (34); here, b indicates the power dependence of the photobleaching rate on the excitation intensity. Thus, the nonlinear dependence of the PA signal on the optical fluence F is more prominent when using a faster photobleaching species (*i.e.*, targets with a higher photobleaching rate b). A more detailed mathematical derivation is provided in the supplementary materials of a previous work [43]. The consistency of the mathematical expressions between the RS-based and PB-based nonlinearities (Eqs. (33) and (34), respectively) indicates an analogous mechanism generating these two nonlinear effects.

2.5.2. Applications

2.5.2.1. Resolution improvement. RS- and PB-based nonlinearities have been applied to improve the lateral and axial resolutions [42,43] of conventional OR-PAM. The two effects operate almost identically in enhancing the spatial resolution; therefore, for simplicity, this review only discusses the results of RS-based nonlinearity.

2.5.2.1.1. Lateral resolution. By substituting the Gaussian distribution of the optical fluence $F(x,y)$ at the focal plane into Eq. (33), we obtain the RS-PAM PA signal at this plane,

$$PA_{RS-PAM}(x,y) \propto \Gamma N_0 F^{bm+1}(x,y) = \frac{\Gamma N_0 E^{bm+1}}{\pi^{m+1} w_0^{2(bm+1)}} exp\left(- \frac{x^2+y^2}{w_0^2/(bm+1)} \right) \tag{35}$$

Thus, the FWHM for RS-PAM is quantified as $(2\sqrt{2\ln 2}w_0/\sqrt{bm+1})$. Compared with the conventional OR-PAM, where the lateral resolution is $2\sqrt{2\ln 2}w_0$ (Eq. (23)), RS-PAM improves the lateral resolution by a factor of $\sqrt{bm+1}$ [42]. This enhancement has been validated by imaging a thin layer of photoswitching protein on a sharp cover glass edge (Fig. 12A and B).

2.5.2.1.2. Axial-resolution. Given that the PA amplitude along the z-axis is an integration of the PA signal in the lateral (x-y) plane, $PA(z)$ along the z-axis in RS-PAM can be obtained by integrating Eq. (33) in the x–y plane,

$$PA_{RS-PAM}(z) \propto \iint \Gamma N_0 F^{bm+1}(x,y,z) dxdy \tag{36}$$

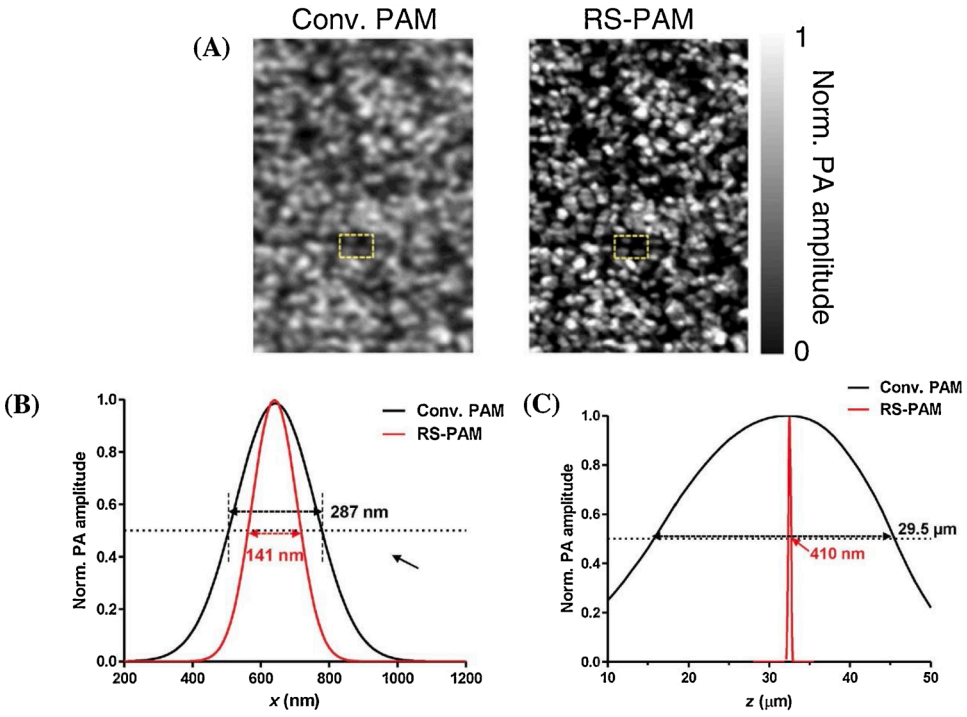

Fig. 12. Validation of the spatial resolution enhancement. **(A)** Conventional OR-PAM and PS-PAM images of a thin layer of protein molecules (BphP1), showing the finer axial resolution of RS-PAM. **(B)** The lateral line spread functions of OR-PAM and RS-PAM; the latter improves $R_{lateral}$ from 278 nm to 141 nm. **(C)** The axial plane spread functions of OR-PAM and RS-PAM. The latter is capable of optical sectioning with an axial resolution of ~410 nm; in contrast, the former's R_{axial} is ~30 μm. Figures reproduced with publisher's permission [42].

Substituting the Gaussian distribution of the optical fluence $F(x,y)$ into Eq. (36) and performing several steps of derivation, the RS-PAM signal for a planar target is given by $PA_{RS-PAM}(z) = \Gamma N_0 E^{bm+1} / \left[(bm+1)\,\pi^{bm+1} w^{2bm}(z)\right]$. Thus, the FWHM of the axial RS-PAM PA signal is estimated as $1.8\sqrt{2^{\frac{1}{bm}}-1}\lambda/NA^2$ [42]. This result indicate that under conditions of $bm>1$, RS-PAM provides axial resolutions even finer than the optically defined axial resolution ($1.8\lambda/NA^2$). This super-resolution has been demonstrated by the measurement of the A-line on a thin layer of protein molecules (Fig. 12C).

2.5.3. Occurrence conditions

Both of the RS-based and PB-based nonlinearities employ the double-excitation process. RS-based nonlinearity exploits the unique photochromic features of genetically encoded probes between two light-absorption states. These features can be found in previous studies for several representative probes, including RpBphP1 and DrBphP [42,119]. These photoswitching probes are required to be either expressed in biological cells or implanted into samples/biological tissues for the nonlinear mechanism to function, as opposed to GR-based nonlinearity which permits a label-free nonlinear mechanism. In PB-based nonlinearity, the inhomogeneous photobleaching is employed to construct a fluence-dependent profile of the absorption coefficient within the optical focal spot using two laser excitations. The PB effect can be identified in a number of absorbing species, including red-dyed microspheres, melanoma, hemoglobin, and pink anthocyanins [43]. PB-based nonlinearity is applicable to both fluorescent and nonfluorescent species [43,121]. For fluorescent species, photobleaching is a form of photochemical destruction of a fluorophore, in which the photobleaching rate exhibits a strong dependence on the excitation intensity [122,123]. For nonfluorescent species, photobleaching is a result of the photothermal destruction of the absorber structure [124]. As reported in a previous study [124], small-sized targets irradiated with short pulse durations more easily suffer photobleaching than the opposite conditions (*i.e.*, large target size and long pulse duration). Because of the aforementioned occurrence conditions, the applicability of the PB effect is limited when compared to GR-based nonlinearity.

2.6. Other types of nonlinearity

As mentioned in the introduction, this review focuses on the above-mentioned six types of nonlinearity as the representative examples, but it is worth mentioning there exist other nonlinear effects in PA imaging, including nano-/microbubble generations [45,46], photochemical reactions [47], the photoacoustic resonance [48–51], unsatisfied stress and thermal confinement [52]. In addition, the nonlinear beamforming (BF) technique [53–59] is another one used in photoacoustic tomography (PAT), which will be briefly discussed here. In PAT, delay and sum (DAS) is the most common beamforming algorithm owing to its straightforward implementation, however, it suffers from strong noises and sidelobes [59,125]. Delay-multiply-and-sum (DMAS) provides a better image quality relative to DAS, but requires high computational cost due to the combinatorial multiplication operations used in DMAS [57,59,126]. A recently developed method, nonlinear *p*th root delay-and-sum (NL-*p*-DAS) [56,127], which is a generalized form of DMAS, utilizes root scaling before and power scaling after the summation, enabling the spatial resolution to be continuously improved as p increases. NL-*p*-DAS has been demonstrated as an effective beamforming technique but still has certain drawbacks [56,128], thus is in the process of being improved [53,129]. The nonlinear BF technique is an interesting topic in PAT and deserves more efforts to reinforce and boost its developments in the future.

3. Summary of the nonlinearity rule

Based on the various nonlinear mechanisms reviewed above, this section summarizes the common relationships between the applications of a nonlinear effect and the specific mathematical structure of its PA amplitude expression. The purpose of this section is to provide guidelines for identifying and inspiring further nonlinearity applications; this is of practical significance in the advancement of nonlinear photoacoustics. Utilization(s) of a nonlinear mechanism can be determined *via* its functional form, in particular, *via* the form of the pulse fluence F and absorption coefficient μ_a. As summarized in Fig. 13, for a mechanism with an ascending power of F, it is expected that nonlinearity can be utilized to achieve super-resolution OR-PAM. Increasing the power on μ_a

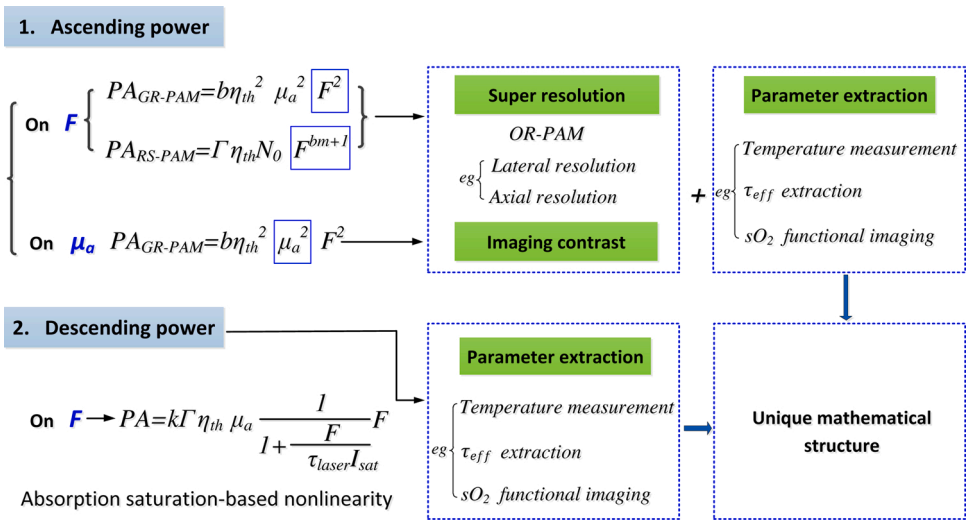

Fig. 13. Conceptual diagram of the correlations between mathematical structure patterns and their application approaches.

increases the imaging contrast. Using the unique mathematical structure (discussed in Section 3.3) of a single parameter in the PA amplitude expression, a nonlinear mechanism can be exploited for parameter extraction procedures such as the measurement of temperature, extraction of relaxation time τ_{eff}, and functional imaging of sO_2. Below are the rules that concern how different nonlinear photoacoustics can be used, and how a particular mathematical structure in the nonlinear mathematical formula can be exploited. When a descending power of F or μ_a occurs, the spatial resolution or image contrast may not be improved. However, other applications (*e.g.*, parameter extraction) can still be realized, provided the mathematical structure of the nonlinearity is suitable to be exploited for that purpose, as will be described in Section 3.3. In this paper, only three applications in parameter extraction (*i.e.*, of temperature, τ_{eff} and sO_2) are considered (see Fig. 13). However, other parameter quantifications might be discovered in the future, using the rules provided in the following sections.

3.1. Ascending / descending power of F

The change in the PA signal power dependence on F typically occurs through the alteration of parameters (k, Γ, η_{th} and μ_a shown in Eq. (1)) in the PA amplitude expression during optical illumination; that is, the dependences of these parameters on the optical fluence F induces the ascending/descending power on F in the PA signal expression. For example, in GR-based nonlinearity, Γ increases during laser irradiation because of the temperature rise, and a dependence of Γ on F is eventually formed (Eq. (20)). Regarding RS- and PB-based nonlinearities, the coefficient of μ_a changes after laser-pulse illumination, owing to the photoswitching and photobleaching effects; this produces a reduction profile μ_a (x,y) governed by $F(x,y)$ (Fig. 1E.3). For thermal-based nonlinearity, the expansion coefficient β (which locates in the expression of Γ) changes with the optical fluence under a significant transient temperature rise, thereby producing the Grueneisen dependence on the optical fluence F (Eqs. (9) and (7)). In absorption-saturation-based nonlinearity, μ_a decreases with increasing optical intensity I, which also forms a dependence on the optical fluence F (Eq. (2)). To summarize, adding extra dependences of these coefficients on the optical fluence F produces an ascending or descending power on F in the PA signal. In the aforementioned nonlinearities, the first three cases produce an ascending power on F, whereas the last one leads to a descending power. Thus, an alteration of the power dependence on F is achieved in the existing nonlinear mechanisms presented in the literature. In particular, an ascending power of F enhances the spatial resolution, as described in the following.

3.1.1. Resolution improvement

3.1.1.1. Lateral resolution. Generally, the lateral resolution of PA imaging is quantified using the FWHM of the PA signal in the lateral plane. For OR-PAM involving an optical focal spot smaller than the acoustic one, the lateral resolution is determined using the optical FWHM of the Gaussian beam distribution on the focal plane. This is because the FWHM of the optical Gaussian beam profile equals the FWHM of the PA signal, provided that the remaining parameters (k, Γ, η_{th}, μ_a) in Eq. (1) are spatially invariant (*i.e.*, constants) within the optical focal spot in the lateral direction. As illustrated in Fig. 14A, the FWHM of a Gaussian distribution multiplied by a constant remains unchanged. However, when the above parameters are not constant within the excitation spot but depend on the optical fluence F, the FWHMs of the Gaussian beam profile and PA signal are no longer equivalent (*e.g.*, in GR- and RS-based nonlinearity, owing to the spatially varying $\Gamma(x,y)$ and μ_a (x, y)). In GR-based nonlinearity, the effective Gruneisen parameter for GR-PAM $\Gamma_{GR-PAM} = \Delta\Gamma(F) \propto F$, shows a linear dependence on the optical fluence, as discussed in Section 2.4.1. In RS-based nonlinearity, the switching properties of protein (between ON and OFF states) generates a reduction profile for the absorption coefficient μ_a, which is governed by the optical Gaussian distribution $F(x, y)$, as illustrated in Fig. 1E.3. In such cases, asides from the original Gaussian spatial profile of the optical beam fluence $F(x, y)$, another Gaussian spatial window characterizing the profile of the F-determined parameters (Γ or μ_a)is added to the PA signal expression, as depicted in the second row in Fig. 14A. Thus, the FWHM of the PA signal significantly decreases and a super-lateral resolution is achieved. Super-resolution is essentially realized through the ascending power on F in the PA signal expression, by constructing an F dependence for the Grueneisen parameter $\Gamma = \Gamma(F)$ or absorption coefficient $\mu_a = \mu_a(F)$. To summarize, the lateral resolution $R_{lateral}$ for OR-PAM with an *N-th* power dependence on the optical fluence F is quantified as,

$$R_{\text{lateral}} = FWHM_{beam} = 2\sqrt{2\ln 2}w \Big/ \sqrt{N} = R_{\text{lateral. linear}} \Big/ \sqrt{N} \tag{37}$$

which improves the resolution of the conventional linear OR-PAM by a factor of $\sqrt{N}$. Likewise, with a descending power on F (*e.g.*, in absorption-saturation-based nonlinearity, where $\mu_a = \mu_a(F) = \frac{\mu_0}{1+F/\tau_{laser}I_{sat}}$, it is reasonable to hypothesize that the lateral resolution of OR-PAM decreases accordingly when F is high enough to enter the nonlinear regime.

3.1.1.2. Axial resolution. In the axial direction, the optical Gaussian

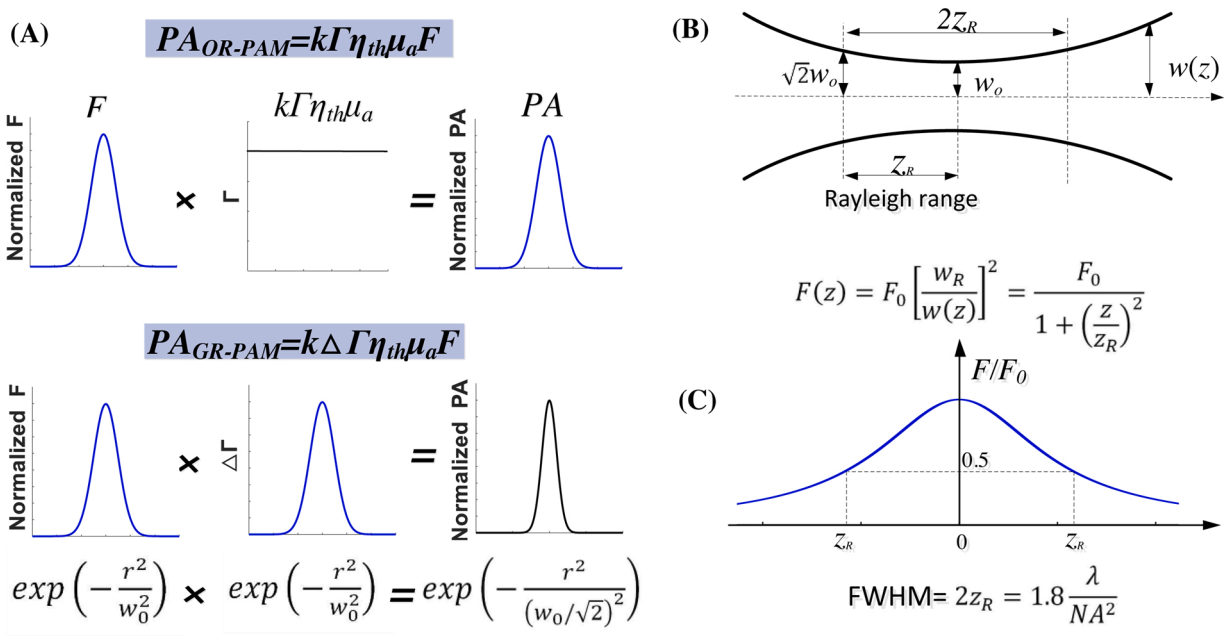

Fig. 14. Principle of the spatial resolution enhancement. **(A)** Illustration of the ascending power of F used to achieve super-lateral resolution. **(B)** Beam focal zone and Rayleigh range. **(C)** The optical fluence profile along the beam axis.

beam converges to and diverges from a planar cross section (*i.e.*, the focal plane) at which the beam radius approaches the beam waist w_0. The spot size (at distance z from the beam waist w_0) expands as a hyperbola (Fig. 14B), and the optical fluence distribution along the beam axis is given by an analytical solution $F(z) = F_0/\left(1+\left(\frac{z}{z_R}\right)^2\right)$, where F_0 denotes the optical fluence at the focal point ($z = 0$) and z_R denotes the Rayleigh range, within which the beam radius w equals $\sqrt{2}\,w_0$ (Fig. 14B, C). According to the expression for $F(z)$, the FWHM of $F(z)$ is estimated as $2z_R = 1.8\lambda/NA^2$ (*i.e.*, twice the Rayleigh range), which is a traditional criterion for defining the optical axial resolution [98,130]. As discussed in Section 2.4.2, the PA signal along the z-axis is given by $\mathrm{PA}(z) = \iint k\Gamma\eta_{th}\mu_a F(x,y,z)dxdy$. For an infinitely small target (*i.e.*, the target size in the lateral plane $\Delta s << $ optical focal spot), $F(x,y,z)$ is considered to be constant inside the infinitesimal region and can be removed by an integration operation. Thus, $\mathrm{PA}(z)$ is expressed as $k\Gamma\eta_{th}\mu_a F(z)\Delta$ s. This means that the FWHM of $\mathrm{PA}(z)$ equals that of $F(z)$, and the optical axial resolution ($1.8\lambda/NA^2$) is achieved using OR-PAM with a point target. However, in general cases, the imaging target is larger than the optical beam spot in the focal zone; hence, it is viewed as a planar target. In such cases, $\mathrm{PA}(z) = k\Gamma\eta_{th}\mu_a E$, according to Equation (25). With no dependence on the optical focal zone, the axial resolution of OR-PAM is decoupled from the optical axial resolution ($1.8\lambda/NA^2$) and consequently determined by the acoustic axial resolution ($R_{axial} = 0.88c/\Delta f$). This acoustic resolution in OR-PAM can be improved by implementing nonlinear mechanisms with a higher-order power of the optical fluence (*e.g.*, GR- or RS-PAM). If an *N-th order* power on the optical fluence F is being constructed, the PA amplitude in the axial axis is given by $\mathrm{PA}(z) = \iint k\Gamma\eta_{th}\mu_a F^N(x,y,z)dxdy$. Based on the iterations discussed in Sections 2.4.2 and 2.5.2, the FWHM of the axial PA signal is expressed as,

$$R_{\text{axial}} = FWHM_{PA.axial} = \frac{1.8\lambda\sqrt{2^{\frac{1}{N-1}}-1}}{NA^2} \ll R_{\text{axial. linear}} \tag{38}$$

As a result, the ascending power of F yields the super-resolution of $\frac{1.8\lambda\sqrt{2^{\frac{1}{N-1}}-1}}{NA^2}$ in the axial direction, which is significantly finer than the axial resolution for linear OR-PAM ($0.88c/\Delta f$). When the power is of order $N > 2$, the nonlinear mechanism's resolution also enhances the optically defined resolution by a factor of $1/\sqrt{2^{\frac{1}{N-1}}-1}$.

3.2. *Ascending/descending power of* μ_a

The ascending/descending power of μ_a primarily arises from the extra dependence of the remaining parameters (k, Γ, η_{th} and F shown in Eq. (1)) on the absorption coefficient μ_a. For example, in both the thermal- and GR-based nonlinearities, dependences of the Grueneisen parameter Γ on the absorption coefficient (*i.e.*, $\Gamma = \Gamma(\mu_a)$) are formed (Eqs. (7) and (9) for thermal-based nonlinearity, Eq. (20) for GR-based nonlinearity). The Grueneisen parameter is generally insensitive to μ_a, because Γ is only subject to the equilibrium temperature ($\Gamma = \Gamma(T)$). However, according to the thermodynamic laws, when an optical-absorption-induced temperature rise ΔT occurs, a correlation between ΔT and the absorption coefficient μ_a is formed (*i.e.*, $\Delta T = Q/\rho C_p \propto \mu_a F/\rho C_p$). This establishes the dependence of Γ on the absorption coefficient μ_a ($\Gamma = \Gamma(T) = \Gamma(T(\mu_a)) = \Gamma(\mu_a)$). This dependence of Γ on μ_a does not occur in linear photoacoustics, because the transient temperature ΔT is negligible compared with the baseline temperature T_0. However, in thermal-based nonlinearity, the dependence of Γ on μ_a is prominent because of the significant temperature rise ΔT induced by the pulse laser. This μ_a -dependence of the Grueneisen parameter Γ also becomes dominant in GR-based nonlinearity, because the baseline temperature T_0 (which is the μ_a -insensitive contribution) is removed by the subtraction between the second and first PA pulses (Eqs. (18) and (19)). This leaves only the μ_a -dependent contribution ($\Delta T = Q/\rho C_p \propto \mu_a F/\rho C_p$). As a result, an extra dependence of the Grueneisen parameter on μ_a is produced. Compared with linear photoacoustics, where the PA signal is proportional to μ_a (Eq. (1)), this newly added dependence of the Grueneisen parameter on μ_a produces the increased power dependence of the PA signal on μ_a. Asides from the Grueneisen parameter Γ, other parameters (*e.g.*, the optical fluence F) may also become dependent on μ_a. For example, the depth-resolved optical fluence is given by $F(z) = F_0 exp(-\mu_a z)$, where F significantly decreases with the depth of target through the optical attenuation (absorption and scattering). With the extra dependence of F on μ_a, the PA signal at the target depth no longer linearly increases with μ_a because the exponential decay term must be accounted for (Eq. (13)); the combined term (*i.e.*, the linear term multiplied by the exponential decay term) can be effectively

regarded as a descending power on μ_a. To conclude, the aforementioned approaches highlight the typical ways in which the ascending/descending power on μ_a is constructed. The ascending power specifically facilitates the increase in imaging contrast, as discussed below.

3.2.1. Imaging contrast enhancement

The ascending power of μ_a is expected to enhance the imaging contrast in PA imaging. For example, in GR-based nonlinearity, a quadratic power dependence on the absorption coefficient μ_a is established (Eq. (21)), which helps realize a better imaging contrast (Fig. 8). The ascending power μ_a causes nonlinear changes in the wavelength dimension; as a result, the PA spectra and absorption spectra are no longer linearly correlated. The ascending power of μ_a functions as an amplification mechanism for the imaging contrast. More specifically, in conventional OR-PAM, absorbing species with high μ_a exhibit a higher PA amplitude than those with low μ_a, and this PA signal difference is determined by the difference in absorbance $(\mu_1 - \mu_2)$. Under an increased power of the absorption coefficient, the difference in PA signal is determined by the power difference $(\mu_1^m - \mu_2^m)$, which produces a considerably higher imaging contrast than the linear OR-PAM. To summarize, the ascending power μ_a^m converts the spectral contrast in absorption spectroscopy to a stronger one in PA spectroscopy *via* a power-law growth; this improves the imaging contrast. Consequently, biological tissues with weak absorption properties (*e.g.*, gelatin, elastin, and lipids, which are difficult to visualize using the linear PA technique because of their low absorption in the visible range) are now expected to be visualized, because a higher imaging contrast than that of the conventional OR-PAM can be achieved. In addition, the aforementioned biological tissues are expected to be made differentiable through the PA technique using this amplification mechanism, owing to the high spectral contrast $(\mu_1^m - \mu_2^m)$ in nonlinear photoacoustics. Conversely, when a decreased power dependence of the PA signal on μ_a occurs, the imaging contrast decreases accordingly.

3.3. Unique structure of a single parameter

Many parameters are associated with the generation of PA signals, because the PA effect involves physical, chemical, and signal detection processes, including optical energy absorption, heat transfer, thermoelastic expansion, pressure wave propagation, and signal detection and acquisition. As a result, PA imaging can reflect numerous properties/parameters, including the optical properties (the optical fluence F and the pulse duration τ_{laser}), absorption properties (the molar absorption coefficient σ_A, number of absorbers N_0, and relative concentrations of different absorbers), thermoelastic properties (the speed of sound c, expansion coefficient β, temperature T, and heat capacity C_P), mechanical properties (the bulk modulus B), and signal detection properties (the detection sensitivity k, and axial resolution of a transducer). These parameters relate to the overall mechanism of the PA effect from the optical absorption to the detected PA amplitude. However, the PA technique is generally employed as an imaging modality, and parameter measurements are not widely applicable in conventional linear PA imaging for the following two reasons. (1) Multiple unknown quantities (*e.g.*, k, Γ, and η_{th} in Eq. (1)) are present in the expression of PA amplitude, and the PA amplitude is a simple product of these parameters. Therefore, the parameters do not possess any uniqueness in the mathematical structure of the PA expression (elaborated upon later in this section). As a result, it is difficult to extract parameters from the PA amplitude. (2) Several parameters (*e.g.*, the saturation intensity I_{sat}, relaxation time τ_{eff}, pulse duration τ_{laser}, axial resolution of the transducer Δz, and tissue temperature T, *etc.*) do not directly relate to the linear expression of the PA amplitude (Eq. (1)); thus, they cannot be determined using the PA technique. The above limitations can be resolved using nonlinear PA effects, because the mathematical expression of PA amplitude is changed by their presence. This produces two typical phenomena. (1) Extra dependences are established on some parameters (*e.g.*, the dependence of PA amplitude on the saturation intensity I_{sat} and relaxation time τ_{eff} in absorption-saturation-based nonlinearity (Section 2.1), and the axial resolution of the transducer Δz in the resolution-dependent nonlinearity (Section 2.3), *etc.*). (2) Special mathematical structures of the parameters are formed instead of the linear correlation (Eq. (1)). Such structures include the reciprocal function (Section 2.1), the parabolic function (Section 2.2), the exponential functions (Section 2.3), and the power functions (Sections 2.4 and 2.5), and so on. These changes allow for parameters to be extracted using the new mathematical structure of the nonlinearity.

3.3.1. Parameter extraction

To be identified, a parameter in a mathematical expression must be unique compared to the other parameters in the PA formula. Thus, either the parameter requires a special structure in the PA amplitude expression, or under a condition that the remaining parameters are known in advance. For example, the measurement of τ_{eff} discussed in Section 2.1.2 requires τ_{eff} to be located in the denominator, as shown by the following equation (here, the remaining parameters $(h, \nu, \tau_{laser}, \sigma_{A0})$ in the denominator are known),

$$PA = k\Gamma\eta_{th}\sigma_{A0}N_0\tau_{laser}I_{sat}\left(1 - \frac{1}{1 + \frac{\sigma_{A0}\tau_{eff}}{h\nu\tau_{laser}}F}\right) \tag{39}$$

The larger the dominator $(1 + \sigma_{A0}\tau_{eff}F/h\nu\tau_{laser})$ is, the faster the PA-fluence curve converges. Thus, $\sigma_{A0}\tau_{eff}/h\nu\tau_{laser}$ can be directly determined by the PA-fluence curve fitting; the same applies for τ_{eff}, which is the only undetermined parameter in the denominator. Without this unique structure pattern, the extraction of τ_{eff} would not be feasible. A counter-example can be found in Eq. (39), in which τ_{eff} also stays in the coefficient of I_{sat} $(I_{sat} = h\nu/\sigma_{A0}\tau_{eff})$. However, I_{sat} does not possess any uniqueness in the expression $k\Gamma\eta_{th}\sigma_{A0}N_0\tau_{laser}I_{sat}$, because the position of I_{sat} does not differ to that of k, Γ, and η_{th}, all of which are unknown parameters. Hence, neither I_{sat} or τ_{eff} can be differentiated from the other parameters using the expression of $k\Gamma\eta_{th}\sigma_{A0}N_0\tau_{laser}I_{sat}$.

This is similar to the GR-effect-based temperature measurement in Section 2.4.2, where the temperature is deduced from Γ. As can be observed from Eq. (1), Γ does not originally possess any uniqueness in the mathematical structure $(PA_1 = k\Gamma\eta_{th}\mu_a F)$ because the role that Γ plays is no different to that of k, μ_a or η_{th}, all of which are unknown for complex biological tissues containing more than one absorbing species. However, with the construction of GR-based nonlinearity, Γ vanishes in Eq. (21), making Γ a unique parameter compared the other unknowns, *i.e.* by dividing Eq. (21) with the square of Eq. (18), the remaining unknowns and temperature-independent parameters are cancelled out (see Eq. (28)), and only the temperature-dependent Γ is preserved. The particular mathematical pattern of Γ allows the tissue temperature to be deduced using this nonlinear structure.

A similar case also pertains in sO_2 measurements. The functional imaging of sO_2 is typically performed using the multi-wavelength method, because the PA spectroscopy $PA(\lambda)$ essentially reflect the absorption spectroscopy $\mu_a(\lambda)$. However, as discussed in Section 2.1.2, this approach requires fluence calibration between different wavelengths, which is difficult to achieve in deep tissue. In some cases, an extra method—the multi-fluence approach—is available to tackle this problem. This method requires a nonlinear correlation between the PA signal and the optical fluence to be established; consequently, multi-fluence can be employed to produce different equations for resolving sO_2. However, this approach does not apply to all nonlinear correlations between the PA signal and the optical fluence: it is only effective when one of two conditions holds. (1) At least one parameter reflecting the difference between HbO_2 and HbR is present in the nonlinear relation (*e.g.*, τ_{eff}, σ_A, and I_{sat}, which differ considerably between HbO_2 and HbR); in other words, the above parameters are highly sensitive to the relative

concentrations of HbO_2 and HbR (*i.e.*, they are functions of sO_2,). (2) The above parameters can be extracted using their own mathematical structure, as discussed above. These criteria are exemplified by the absorption-saturation-based nonlinearity, where the difference between HbO_2 and HbR is reflected by the saturated intensity I_{sat} (*i.e.*, the saturation intensity I_{sat} of blood is subject to the relative concentrations of HbO_2 and HbR; thus, $I_{sat} = I_{sat}$ (sO_2)). In Eq. (4), I_{sat} is located in the denominator and represents the curve convergence rate, and the remaining parameters in the denominator are known (see Eq. (4)). Thus, I_{sat} can be directly extracted by fitting the theoretical PA-fluence curve to the experimental curve, using I_{sat} as the free parameter; then, sO_2 can be determined from the relation $I_{sat} = I_{sat}$ (sO_2). The above criteria are also proved by a counter-example: GR-based nonlinearity. The PA signal in GR-based nonlinearity is given by $PA_{GR} = kb\eta_{th}^2\mu_a^2F^2$, where μ_a is the parameter describing the divergence between HbO_2 and HbR. However, μ_a possesses no unique structure compared with k and η_{th}, both of which are unknown; therefore, sO_2 cannot be determined. In other words, sO_2 cannot be quantified using the multi-fluence method with the nonlinearity form (Eq. (21)) in GR-based nonlinearity. The above concept is useful in identifying whether a nonlinear correlation can be applied to the functional image of sO_2 using the single-wavelength method.

4. Conclusion and outlook

Efforts have been made in the past to understand nonlinear photoacoustics and explore methods of exploiting its mechanisms for different purposes. In this review, nonlinear photoacoustics were separated into two categories: single-PA-signal-based nonlinearity (Sections 2.1, 2.2, and 2.3) and double-excitation-based nonlinearity (Sections 2.4 and 2.5). These nonlinear mechanisms have been demonstrated as powerful tools for improving spatial resolution, enhancing imaging contrast, measuring tissue temperature, facilitating functional imaging, extracting important parameters, and discriminating different absorbers. This article reviewed different nonlinear mechanisms in photoacoustics and addressed three topic areas related to each of these nonlinearities: (a) fundamental principles, (b) relevant applications, and (c) occurrence conditions. By applying the occurrence conditions, we can establish a specific nonlinearity to realize the corresponding applications discussed above. Likewise, nonlinearity can be avoided by appropriately re-tuning the influencing parameters of the nonlinear dependences. This was analyzed in detail in the review.

To facilitate further applications, we discussed and summarized the nonlinearity rule concerning the association of a nonlinear dependence's mathematical structure with its practical applications. Based on the analysis, the following are concluded. (1) With an ascending power of the optical fluence, super-resolution can be achieved. (2) With an ascending power of μ_a, the imaging contrast is expected to be improved. (3) The unique mathematical structure of a parameter allows parameter extraction using the PA technique. In particular, functional imaging of sO_2 can be achieved using the single-wavelength method, provided the extracted parameter can reveal difference between HbO_2 and HbR. To the best of our knowledge, the above conclusions are derived here for the first time and demonstrated in this review with precise mathematical reasoning. These summarized nonlinearity rules are particularly useful for identifying potential applications *via* their mathematical expressions; this has practical significance for future advances in nonlinear photoacoustics.

From a mathematical and physical perspective, the recent developments in nonlinearity outline a major pattern concerning the way in which nonlinearities are typically constructed: by manipulating the three main factors (μ_a, F, and Γ) in Eq. (1) to alter the linear correlation between the PA signal and the optical fluence F, and also between the PA signal and absorption coefficient μ_a. Several directions are available for potential future explorations and advances in nonlinear photoacoustics: (1) existing nonlinear mechanisms could be explored for new applications besides those summarized in this review; (2) further nonlinear phenomena and mechanisms are expected to be discovered or established, preferentially the label free ones and also those which help tackle the challenge of low SNR that occur in deep tissues. The local fluence decreases significantly in deep samples, making it difficult to reach the nonlinear regime for absorption saturation-based nonlinearity (Section 2.1); this also restrains the manifestation of a detectable PA signal difference between the two pulses in GR-based nonlinearity (Section 2.4) and the two states in both RS-based and PB-based nonlinearities (Section 2.5) for deep scattering tissues. Future improvements can be made by combining optical focusing methods, to realize precise light delivery to deep organs. The wavefront-shaping technique can be employed to expand the applications of nonlinear photoacoustics *in vivo*. Furthermore, nonlinear mechanisms using the phase-domain photoacoustic sensing [131] may provide new avenues of nonlinear applications. This is because the nonlinear photoacoustics not only induces PA amplitude enhancement, but also phase change. The phase-domain detection, which has been demonstrated to offer higher detection reliability [131] than the conventional time-domain PA method, would be very attractive to consider in future studies.

Funding

National Natural Science Foundation of China (81927807, 92059108); Chinese Academy of Sciences (2019352, YJKYYQ20190078, GJJSTD20210003); Shenzhen Science and Technology Innovation Grant (JCYJ20200109141222892); National Key R&D Program of China (2020YFA0908800); CAS Key Laboratory of Health Informatics (2011DP173015); Guangdong Provincial Key Laboratory of Biomedical Optical Imaging (2020B121201010); Shenzhen Key Laboratory for Molecular Imaging (ZDSY20130401165820357).

Declaration of Competing Interest

The authors declare that there are no conflicts of interest.

References

[1] L.V. Wang, S. Hu, Photoacoustic tomography: in vivo imaging from organelles to organs, Science 335 (6075) (2012) 1458–1462.
[2] H. Song, E. Gonzales, B. Soetikno, E. Gong, L.V. Wang, Optical-resolution photoacoustic microscopy of ischemic stroke, Proc SPIE 7899 (2011), p. 789906-789906-5.
[3] X. Wang, Y. Pang, G. Ku, X. Xie, G. Stoica, L.V. Wang, Noninvasive laser-induced photoacoustic tomography for structural and functional in vivo imaging of the brain, Nat. Biotechnol. 21 (7) (2003).
[4] H.F. Zhang, K. Maslov, L.V. Wang, In vivo imaging of subcutaneous structures using functional photoacoustic microscopy, Nat. Protoc. 2 (4) (2007) 797–804.
[5] Y. Jiang, K. Pu, Advanced photoacoustic imaging applications of near-infrared absorbing organic nanoparticles, Small (2017) 1700710.
[6] C. Zhang, R. Gao, L. Zhang, C. Liu, Z. Yang, S. Zhao, Design and synthesis of a ratiometric photoacoustic probe for in situ imaging of zinc ions in deep tissue in vivo, Anal. Chem. 92 (9) (2020) 6382–6390.
[7] A.B.E. Attia, G. Balasundaram, M. Moothanchery, U. Dinish, R. Bi, V. Ntziachristos, M. Olivo, A review of clinical photoacoustic imaging: current and future trends, Photoacoustics (2019) 100144.
[8] Q. Chen, T. Yin, Y. Bai, X. Miao, R. Gao, H. Zhou, R. Jie, L. Song, C. Liu, H. Zheng, R. Zheng, Targeted imaging of orthotopic prostate cancer by using clinical transformable photoacoustic molecular probe, BMC Cancer 20 (2020) 1–10.
[9] C. Kim, E.C. Cho, J. Chen, K.H. Song, L. Au, C. Favazza, Q. Zhang, C.M. Cobley, F. Gao, Y. Xia, In vivo molecular photoacoustic tomography of melanomas targeted by bioconjugated gold nanocages, ACS Nano 4 (8) (2010) 4559–4564.
[10] H.-C. Zhou, N. Chen, H. Zhao, T. Yin, J. Zhang, W. Zheng, L. Song, C. Liu, R. Zheng, Optical-resolution photoacoustic microscopy for monitoring vascular normalization during anti-angiogenic therapy, Photoacoustics 15 (2019) 100143.
[11] K. Jansen, A.F.W. van der Steen, H.M.M. van Beusekom, J.W. Oosterhuis, G. van Soest, Intravascular photoacoustic imaging of human coronary atherosclerosis, Opt. Lett. 36 (5) (2011) 597–599.
[12] S. Hu, L. Wang, Neurovascular photoacoustic tomography, Front. Neuroenerg. 2 (2010) 10.
[13] S. Hu, P. Yan, K. Maslov, J.-M. Lee, L.V. Wang, Intravital imaging of amyloid plaques in a transgenic mouse model using optical-resolution photoacoustic microscopy, Opt. Lett. 34 (24) (2009) 3899–3901.

[14] X. Wang, Y. Pang, G. Ku, X. Xie, G. Stoica, L.V. Wang, Noninvasive laser-induced photoacoustic tomography for structural and functional in vivo imaging of the brain, Nat. Biotechnol. 21 (7) (2003) 803–806.

[15] H. Li, P. Zhang, L.P. Smaga, R.A. Hoffman, J. Chan, Photoacoustic probes for ratiometric imaging of copper (II), J. Am. Chem. Soc. 137 (50) (2015) 15628–15631.

[16] B. Ning, M.J. Kennedy, A.J. Dixon, N. Sun, R. Cao, B.T. Soetikno, R. Chen, Q. Zhou, K.K. Shung, J.A. Hossack, Simultaneous photoacoustic microscopy of microvascular anatomy, oxygen saturation, and blood flow, Opt. Lett. 40 (6) (2015) 910–913.

[17] M. Schwarz, A. Buehler, J. Aguirre, V. Ntziachristos, Three-dimensional multispectral optoacoustic mesoscopy reveals melanin and blood oxygenation in human skin in vivo, J. Biophotonics 9 (1-2) (2016) 55–60.

[18] J. Yao, K.I. Maslov, Y. Zhang, Y. Xia, L.V. Wang, Label-free oxygen-metabolic photoacoustic microscopy in vivo, J. Biomed. Opt. 16 (7) (2011) 076003.

[19] L.V. Wang, H.-i. Wu, Biomedical Optics: Principles and Imaging, John Wiley & Sons, 2012.

[20] Zhou Yong, Yao Junjie, Lihong, Wang, Tutorial on photoacoustic tomography, J. Biomed. Opt. 21 (6) (2016).

[21] P. Repond, M.W. Sigrist, Photoacoustic spectroscopy on trace gases with continuously tunable CO2 laser, Appl. Opt. 35 (21) (1996) 4065–4085.

[22] A.-M.B. Magureanu, C. Popa, Laser photoacoustic spectroscopy principles, instrumentation, and characterization, J. Optoelectron. Adv. Mater. 9 (12) (2007) 3655.

[23] A. Danielli, C.P. Favazza, K. Maslov, L.V. Wang, Picosecond absorption relaxation measured with nanosecond laser photoacoustics, Appl. Phys. Lett. 97 (16) (2010) 163701.

[24] A. Danielli, C.P. Favazza, K. Maslov, L.V. Wang, Single-wavelength functional photoacoustic microscopy in biological tissue, Opt. Lett. 36 (5) (2011) 769–771.

[25] A. Danielli, K. Maslov, C.P. Favazza, J. Xia, L.V. Wang, Nonlinear photoacoustic spectroscopy of hemoglobin, Appl. Phys. Lett. 106 (20) (2015) 203701.

[26] V.B. Oshurko, Imaging thermal fields in nonlinear photoacoustics, Tech. Phys. Lett. 32 (8) (2006) 691–693.

[27] S.V. Egerev, A.A. Oraevsky, Optothermoacoustic phenomena in highly diluted suspensions of gold nanoparticles, Int. J. Thermophys. 29 (6) (2008) 2116–2125.

[28] S.Y. Nam, L.M. Ricles, L.J. Suggs, S.Y. Emelianov, Nonlinear photoacoustic signal increase from endocytosis of gold nanoparticles, Opt. Lett. 37 (22) (2012) 4708–4710.

[29] I.G. Calasso, W. Craig, G.J. Diebold, Photoacoustic point source, Phys. Rev. Lett. 86 (16) (2001) 3550–3553.

[30] O. Simandoux, A. Prost, J. Gateau, E. Bossy, Influence of nanoscale temperature rises on photoacoustic generation: discrimination between optical absorbers based on thermal nonlinearity at high frequency, Photoacoustics 3 (1) (2015) 20–25.

[31] G.A. Pang, J. Laufer, R. Niessner, C. Haisch, Photoacoustic signal generation in gold nanospheres in aqueous solution: signal generation enhancement and particle diameter effects, J. Phys. Chem. C 120 (48) (2016) 27646–27656.

[32] S. Schrof, G. Pang, J. Buchmann, J. Laufer, Exploiting nonlinear photoacoustic signal generation in gold nanospheres for selective detection in serial 3D PA tomography, J. Imaging 4 (12) (2018).

[33] J. Wang, T. Liu, S. Jiao, R. Chen, Q. Zhou, K.K. Shung, L.V. Wang, H.F. Zhang, Saturation effect in functional photoacoustic imaging, J. Biomed. Opt. 15 (2) (2010) 021317.

[34] C. Liu, Y. Liang, L. Wang, Optical-resolution photoacoustic microscopy of oxygen saturation with nonlinear compensation, Biomed. Opt. Express 10 (6) (2019) 3061–3069.

[35] M. Sivaramakrishnan, K. Maslov, H.F. Zhang, G. Stoica, L.V. Wang, Limitations of quantitative photoacoustic measurements of blood oxygenation in small vessels, Phys. Med. Biol. 52 (5) (2007) 1349.

[36] L. Wang, C. Zhang, L.V. Wang, Grueneisen relaxation photoacoustic microscopy, Phys. Rev. Lett. 113 (17) (2014) 174301.

[37] X. Liu, T.T. Wong, J. Shi, J. Ma, Q. Yang, L.V. Wang, Label-free cell nuclear imaging by Grüneisen relaxation photoacoustic microscopy, Opt. Lett. 43 (4) (2018) 947–950.

[38] J. Ma, J. Shi, P. Hai, Y. Zhou, L.V. Wang, Grueneisen relaxation photoacoustic microscopy in vivo, J. Biomed. Opt. 21 (6) (2016) 066005.

[39] Y. Zhou, M. Li, W. Liu, G. Sankin, J. Luo, P. Zhong, J. Yao, Thermal memory based photoacoustic imaging of temperature, Optica 6 (2) (2019) 198–205.

[40] J. Shi, L. Wang, C. Noordam, L. Wang, Bessel-beam Grueneisen relaxation photoacoustic microscopy with extended depth of field, J. Biomed. Opt. 20 (11) (2015) 116002.

[41] P. Lai, L. Wang, J.W. Tay, L.V. Wang, Photoacoustically guided wavefront shaping for enhanced optical focusing in scattering media, Nat. Photonics 9 (2) (2015) 126–132.

[42] J. Yao, A.A. Kaberniuk, L. Li, D.M. Shcherbakova, R. Zhang, L. Wang, G. Li, V. V. Verkhusha, L.V. Wang, Multiscale photoacoustic tomography using reversibly switchable bacterial phytochrome as a near-infrared photochromic probe, Nat. Methods 13 (1) (2016) 67–73.

[43] J. Yao, L. Wang, C. Li, C. Zhang, L.V. Wang, Photoimprint photoacoustic microscopy for three-dimensional label-free subdiffraction imaging, Phys. Rev. Lett. 112 (1) (2014) 014302.

[44] J. Yao, L. Wang, J.-M. Yang, K.I. Maslov, T.T. Wong, L. Li, C.-H. Huang, J. Zou, L. V. Wang, High-speed label-free functional photoacoustic microscopy of mouse brain in action, Nat. Methods 12 (5) (2015) 407–410.

[45] D. Lapotko, Plasmonic nanoparticle-generated photothermal bubbles and their biomedical applications, Nanomedicine 4 (7) (2009) 813–845.

[46] S. Mustafa, A.N. Dmitry, A.M. Yulian, A.J. Mazen, P.Z. Vladimir, Nonlinear photoacoustic signal amplification from single targets in absorption background, Photoacoustics 2 (1) (2014) 1–11.

[47] M.T. O"Connor, G.J. Diebold, Chemical amplification of optoacoustic signals, Nature 301 (5898) (1983) 321–322.

[48] F. Gao, X. Feng, Y. Zheng, C.-D. Ohl, Photoacoustic resonance spectroscopy for biological tissue characterization, J. Biomed. Opt. 19 (6) (2014) 067006.

[49] F. Gao, X. Feng, Y. Zheng, Photoacoustic elastic oscillation and characterization, Opt. Express 23 (16) (2015) 20617–20628.

[50] D. Kang, B. Lashkari, A. Mandelis, Photoacoustic resonance by spatial filtering of focused ultrasound transducers, Opt. Lett. 42 (4) (2017) 655–658.

[51] R. Zhang, F. Gao, X. Feng, S. Liu, R. Ding, Y. Zheng, Photoacoustic resonance imaging, Ieee J. Sel. Top. Quantum Electron. 25 (1) (2019) 1–7.

[52] F. Gao, X. Feng, R. Zhang, S. Liu, R. Ding, R. Kishor, Y. Zheng, Single laser pulse generates dual photoacoustic signals for differential contrast photoacoustic imaging, Sci. Rep. 7 (1) (2017) 626.

[53] S. Cho, S. Jeon, W. Choi, R. Managuli, C. Kim, Nonlinear pth root spectral magnitude scaling beamforming for clinical photoacoustic and ultrasound imaging, Opt. Lett. 45 (16) (2020) 4575–4578.

[54] W. Choi, D. Oh, C. Kim, Practical photoacoustic tomography: realistic limitations and technical solutions, J. Appl. Phys. 127 (23) (2020) 230903.

[55] S. Jeon, E.-Y. Park, W. Choi, R. Managuli, K.j. Lee, C. Kim, Real-time delay-multiply-and-sum beamforming with coherence factor for in vivo clinical photoacoustic imaging of humans, Photoacoustics 15 (2019) 100136.

[56] M. Mozaffarzadeh, V. Periyasamy, M. Pramanik, B. Makkiabadi, Efficient nonlinear beamformer based on P'th root of detected signals for linear-array photoacoustic tomography: application to sentinel lymph node imaging, J. Biomed. Opt. 23 (12) (2018) 121604.

[57] M. Mozaffarzadeh, A. Hariri, C. Moore, J.V. Jokerst, The double-stage delay-multiply-and-sum image reconstruction method improves imaging quality in a LED-based photoacoustic array scanner, Photoacoustics 12 (2018) 22–29.

[58] M. Fournelle, W. Bost, Wave front analysis for enhanced time-domain beamforming of point-like targets in optoacoustic imaging using a linear array, Photoacoustics 14 (2019) 67–76.

[59] M. Mozaffarzadeh, A. Mahloojifar, M. Orooji, K. Kratkiewicz, S. Adabi, M. Nasiriavanaki, Linear-array photoacoustic imaging using minimum variance-based delay multiply and sum adaptive beamforming algorithm, J. Biomed. Opt. 23 (2) (2018) 026002.

[60] F. Gao, X. Feng, Y. Zheng, Advanced photoacoustic and thermoacoustic sensing and imaging beyond pulsed absorption contrast, J. Opt. 18 (7) (2016) 074006.

[61] A.E. Siegman, Lasers, vol. 37, University Science Books, Mill Valley, CA, 1986 (208): p. 169.

[62] R. Berera, R. van Grondelle, J.T.M. Kennis, Ultrafast transient absorption spectroscopy: principles and application to photosynthetic systems, Photosyn. Res. 101 (2–3) (2009) 105–118.

[63] Z. Chen, J.A. Stevens, J.J. Link, L. Guo, L. Wang, D. Zhong, Ultrafast proteinquake dynamics in cytochrome c, J. Am. Chem. Soc. 131 (8) (2009) 2846.

[64] T. Dartigalongue, C. Niezborala, F.O. Hache, Subpicosecond UV spectroscopy of carbonmonoxy-myoglobin: absorption and circular dichroism studies, J. Chem. Soc. Faraday Trans. 9 (13) (2007) 1611–1615.

[65] W. Demtröder, Laser Spectroscopy: Vol. 2: Experimental Techniques, Springer Science & Business Media, 2008. Chapter 6.

[66] G. Statkutė, I. Mikulskas, R. Tomašiūnas, A. Jagminas, Near-IR absorption saturation and mechanism of picosecond recovery dynamics of copper selenide nanostructured via alumina, J. Appl. Phys. 105 (11) (2009) 113519.

[67] S. Gayen, W. Wang, V. Petričević, K. Yoo, R. Alfano, Picosecond excite-and-probe absorption measurement of the intra-2 E g E 3/2-state vibrational relaxation time in Ti3+: Al2O3, Appl. Phys. Lett. 50 (21) (1987) 1494–1496.

[68] S. Sauvage, P. Boucaud, F. Glotin, R. Prazeres, J.-M. Ortega, A. Lemaıtre, J.-M. Gérard, V. Thierry-Flieg, Saturation of intraband absorption and electron relaxation time in n-doped InAs/GaAs self-assembled quantum dots, Appl. Phys. Lett. 73 (26) (1998) 3818–3821.

[69] S. Palfrey, T.F. Heinz, Coherent interactions in pump–probe absorption measurements: the effect of phase gratings, JOSA B 2 (4) (1985) 674–679.

[70] M. Li, Y. Tang, J. Yao, Photoacoustic tomography of blood oxygenation: a mini review, Photoacoustics 10 (2018) 65–73.

[71] B.T. Cox, J.G. Laufer, P.C. Beard, S.R. Arridge, Quantitative spectroscopic photoacoustic imaging: a review, J. Biomed. Opt. 17 (6) (2012) 061202.

[72] M.-L. Li, J.-T. Oh, X. Xie, G. Ku, W. Wang, C. Li, G. Lungu, G. Stoica, L.V. Wang, Simultaneous molecular and hypoxia imaging of brain tumors in vivo using spectroscopic photoacoustic tomography, Proc. IEEE 96 (3) (2008) 481–489.

[73] J. Laufer, C. Elwell, D. Delpy, P. Beard, In vitro measurements of absolute blood oxygen saturation using pulsed near-infrared photoacoustic spectroscopy: accuracy and resolution, Phys. Med. Biol. 50 (18) (2005) 4409.

[74] Z. Chen, S. Yang, D. Xing, In vivo detection of hemoglobin oxygen saturation and carboxyhemoglobin saturation with multiwavelength photoacoustic microscopy, Opt. Lett. 37 (16) (2012) 3414–3416.

[75] A. Hussain, W. Petersen, J. Staley, E. Hondebrink, W. Steenbergen, Quantitative blood oxygen saturation imaging using combined photoacoustics and acousto-optics, Opt. Lett. 41 (8) (2016) 1720–1723.

[76] J. Laufer, D. Delpy, C. Elwell, P. Beard, Quantitative spatially resolved measurement of tissue chromophore concentrations using photoacoustic spectroscopy: application to the measurement of blood oxygenation and haemoglobin concentration, Phys. Med. Biol. 52 (1) (2006) 141.

[77] J. Xia, A. Danielli, Y. Liu, L. Wang, K. Maslov, L.V. Wang, Calibration-free quantification of absolute oxygen saturation based on the dynamics of photoacoustic signals, Opt. Lett. 38 (15) (2013) 2800–2803.
[78] K. Sei, M. Fujita, T. Hirasawa, S. Okawa, T. Kushibiki, H. Sasa, K. Furuya, M. Ishihara, Measurement of blood-oxygen saturation using a photoacoustic technique in the rabbit hypoxemia model, J. Clin. Monit. Comput. 33 (2) (2019) 269–279.
[79] F. Gao, P. Q, F. X, G. B, Z. Y, Single-wavelength blood oxygen saturation sensing with combined optical absorption and scattering, IEEE Sens. J. 16 (7) (2016) 1943–1948.
[80] University of California, M, Laser Safety Manual, 2011.
[81] A. Prost, F. Poisson, E. Bossy, Photoacoustic generation by a gold nanosphere: from linear to nonlinear thermoelastics in the long-pulse illumination regime, Phys. Rev. B 92 (11) (2015) 115450.
[82] J. Shah, S. Park, S. Aglyamov, T. Larson, M. Li, K. Sokolov, K. Johnston, T. Milner, S.Y. Emelianov, Photoacoustic imaging and temperature measurement for photothermal cancer therapy, J. Biomed. Opt. 13 (3) (2008) 417–425.
[83] D.R. Lide, CRC Handbook of Chemistry and Physics - 80th Edition 1999–2000, Crc Press, 1999, 15 (7): p. 504.
[84] X. Huang, P.K. Jain, I.H. El-Sayed, M.A. El-Sayed, Plasmonic photothermal therapy (PPTT) using gold nanoparticles, Lasers Med. Sci. 23 (3) (2008) 217.
[85] X. Huang, M.A. El-Sayed, Gold nanoparticles: optical properties and implementations in cancer diagnosis and photothermal therapy, J. Adv. Res. 1 (1) (2010) 13–28.
[86] I.H. El-Sayed, X. Huang, M.A. El-Sayed, Selective laser photo-thermal therapy of epithelial carcinoma using anti-EGFR antibody conjugated gold nanoparticles, Cancer Lett. 239 (1) (2006) 129–135.
[87] Y.-S. Chen, W. Frey, S. Aglyamov, S. Emelianov, Environment-dependent generation of photoacoustic waves from plasmonic nanoparticles, Small 8 (1) (2012) 47–52.
[88] T. Fukasawa, S. Noguchi, H. Shinto, H. Aoki, S. Ito, M. Ohshima, Effects of physicochemical properties of particles and medium on acoustic pressure pulses from laser-irradiated suspensions, Colloids Surf. A Physicochem. Eng. Asp. 487 (2015) 42–48.
[89] H. Shinto, T. Fukasawa, H. Aoki, S. Ito, M. Ohshima, Acoustic pressure pulsesfrom laser-irradiated suspensions containing gold nanospheres in water:experimental and theoretical study, Colloids Surf. A Physicochem. Eng. Asp. 430 (2013) 51–57.
[90] C.-w. Wei, M. Lombardo, K. Larson-Smith, I. Pelivanov, C. Perez, J. Xia, T. Matula, D. Pozzo, M. O'Donnell, Nonlinear contrast enhancement in photoacoustic molecular imaging with gold nanosphere encapsulated nanoemulsions, Appl. Phys. Lett. 104 (3) (2014) 033701.
[91] R. Hochuli, P.C. Beard, B. Cox, Effect of wavelength selection on the accuracy of blood oxygen saturation estimates obtained from photoacoustic images, in: Photons Plus Ultrasound: Imaging and Sensing, International Society for Optics and Photonics, 2015.
[92] C. Lee, M. Jeon, M.Y. Jeon, J. Kim, C. Kim, In vitro photoacoustic measurement of hemoglobin oxygen saturation using a single pulsed broadband supercontinuum laser source, Appl. Opt. 53 (18) (2014) 3884–3889.
[93] C.-S. Friedrich, M.P. Mienkina, C. Brenner, N.C. Gerhardt, M. Jörger, A. Strauß, M.F. Beckmann, G. Schmitz, M.R. Hofmann, Photoacoustic blood oxygenation imaging based on semiconductor lasers, Photonics Optoelect 1 (2012) 48–54.
[94] N.E. Everds, Hematology of the laboratory mouse. The Mouse in Biomedical Research, Elsevier, 2007, p. 133-XVIII.
[95] I.V. Larina, K.V. Larin, R.O. Esenaliev, Real-time optoacoustic monitoring of temperature in tissues, J. Phys. D Appl. Phys. 38 (15) (2005) 2633–2639.
[96] M. Xu, L.V. Wang, Photoacoustic imaging in biomedicine, Rev. Sci. Instrum. 77 (4) (2006) 305–598.
[97] D. Meschede, Optics, Light and Lasers: the Practical Approach to Modern Aspects of Photonics and Laser Physics, John Wiley & Sons, 2017.
[98] J. Squier, M. Müller, High resolution nonlinear microscopy: a review of sources and methods for achieving optimal imaging, Rev. Sci. Instrum. 72 (7) (2001) 2855–2867.
[99] C.L. Arnold, S. Akturk, A. Mysyrowicz, V. Jukna, A. Couairon, T. Itina, R. Stoian, C. Xie, J.M. Dudley, F. Courvoisier, S. Bonanomi, O. Jedrkiewicz, P.D. Trapani, Nonlinear Bessel vortex beams for applications, J. Phys. B At. Mol. Opt. Phys. 48 (9) (2015) 094006.
[100] F. Gao, X. Feng, R. Zhang, S. Liu, R. Ding, R. Kishor, Y. Zheng, Single laser pulse generates dual photoacoustic signals for differential contrast photoacoustic imaging, Sci. Rep. 7 (1) (2017) 1–12.
[101] Y. Zhou, L. Zhai, R. Simmons, P. Zhong, Measurement of high intensity focused ultrasound fields by a fiber optic probe hydrophone, J. Acoust. Soc. Am. 120 (2) (2006) 676.
[102] M. Alaeian, H.R.B. Orlande, Inverse photoacoustic technique for parameter and temperature estimation in tissues, Heat Transf. Eng. 38 (18) (2017) 1573–1594.
[103] M. Pramanik, L.V. Wang, Thermoacoustic and photoacoustic sensing of temperature, J. Biomed. Opt. 14 (5) (2009) 054024.
[104] M. Pramanik, T.N. Erpelding, L. Jankovic, L.V. Wang, Tissue temperature monitoring using thermoacoustic and photoacoustic techniques, Proc. SPIE 7564 (6) (2010), p. 75641Y-75641Y-10.
[105] L. Gao, L. Wang, C. Li, Y. Liu, H. Ke, C. Zhang, L.V. Wang, Single-cell photoacoustic thermometry, J. Biomed. Opt. 18 (2) (2013) 026003.
[106] F. Xiaohua, G. Fei, Z. Yuanjin, Photoacoustic-based-close-loop temperature control for nanoparticle hyperthermia, IEEE Trans. Biomed. Eng. 62 (7) (2015) 1728–1737.
[107] X. Feng, F. Gao, C. Xu, L. Gaoming, Y. Zheng, Self temperature regulation of photothermal therapy by laser-shared photoacoustic feedback, Opt. Lett. 40 (19) (2015) 4492–4495.
[108] T. Duan, H. Lan, H. Zhong, M. Zhou, R. Zhang, F. Gao, Hybrid multi-wavelength nonlinear photoacoustic sensing and imaging, Opt. Lett. 43 (22) (2018) 5611–5614.
[109] H. Zhong, D. Jiang, H. Lan, T. Duan, F. Gao, F. Gao, Low-cost multi-wavelength photoacoustic imaging based on portable continuous-wave laser diode module, IEEE Trans. Biomed. Circ. Syst. 14 (4) (2020) 738–745.
[110] J. Shi, T.T. Wong, Y. He, L. Li, R. Zhang, C.S. Yung, J. Hwang, K. Maslov, L. V. Wang, High-resolution, high-contrast mid-infrared imaging of fresh biological samples with ultraviolet-localized photoacoustic microscopy, Nat. Photonics 13 (9) (2019) 609–615.
[111] K. Basak, X.L. Deán-Ben, S. Gottschalk, M. Reiss, D. Razansky, Non-invasive determination of murine placental and foetal functional parameters with multispectral optoacoustic tomography, Light Sci. Appl. 8 (1) (2019) 1–10.
[112] D. Razansky, M. Distel, C. Vinegoni, R. Ma, N. Perrimon, R.W. Köster, V. Ntziachristos, Multispectral opto-acoustic tomography of deep-seated fluorescent proteins in vivo, Nat. Photonics 3 (7) (2009) 412–417.
[113] C. Tian, Z. Xie, M.L. Fabiilli, X. Wang, Imaging and sensing based on dual-pulse nonlinear photoacoustic contrast: a preliminary study on fatty liver, Opt. Lett. 40 (10) (2015) 2253–2256.
[114] H. Lan, T. Duan, D. Jiang, H. Zhong, M. Zhou, F. Gao, Dual-contrast nonlinear photoacoustic sensing and imaging based on single high-repetition- rate pulsed laser, IEEE Sens. J. 19 (14) (2019) 5559–5565.
[115] X. Feng, F. Gao, Y. Zheng, Thermally modulated photoacoustic imaging with super-paramagnetic iron oxide nanoparticles, Opt. Lett. 39 (12) (2014) 3414–3417.
[116] F. Gao, L. Bai, X. Feng, H.P. Tham, R. Zhang, Y. Zhang, S. Liu, L. Zhao, Y. Zheng, Y. Zhao, Remarkable in vivo nonlinear photoacoustic imaging based on near-infrared organic dyes, Small 12 (38) (2016) 5239–5244.
[117] F. Gao, L. Bai, S. Liu, R. Zhang, J. Zhang, X. Feng, Y. Zheng, Y. Zhao, Rationally encapsulated gold nanorods improving both linear and nonlinear photoacoustic imaging contrast in vivo, Nanoscale 9 (1) (2017) 79–86.
[118] C. Tian, Z. Xie, M.L. Fabiilli, S. Liu, C. Wang, Q. Cheng, X. Wang, Dual-pulse nonlinear photoacoustic technique: a practical investigation, Biomed. Opt. Express 6 (8) (2015) 2923–2933.
[119] L. Li, A.A. Shemetov, M. Baloban, P. Hu, L. Zhu, D.M. Shcherbakova, R. Zhang, J. Shi, J. Yao, L.V. Wang, Small near-infrared photochromic protein for photoacoustic multi-contrast imaging and detection of protein interactions in vivo, Nat. Commun. 9 (1) (2018) 1–14.
[120] J. Märk, H. Dortay, A. Wagener, E. Zhang, J. Buchmann, C. Grötzinger, T. Friedrich, J. Laufer, Dual-wavelength 3D photoacoustic imaging of mammalian cells using a photoswitchable phytochrome reporter protein, Commun. Phys. 1 (1) (2018) 1–10.
[121] H.F. Launer, Photobleaching—a common phenomenon, Nature 218 (5137) (1968) 160–161.
[122] G.H. Patterson, D.W. Piston, Photobleaching in two-photon excitation microscopy, Biophys. J. 78 (4) (2000) 2159–2162.
[123] T.-S. Chen, S.-Q. Zeng, Q.-M. Luo, Z.-H. Zhang, W. Zhou, High-order photobleaching of green fluorescent protein inside live cells in two-photon excitation microscopy, Biochem. Biophys. Res. Commun. 291 (5) (2002) 1272–1275.
[124] L. Gao, L. Wang, C. Li, A. Garcia-Uribe, L.V. Wang, Photothermal bleaching in time-lapse photoacoustic microscopy, J. Biophotonics 6 (6–7) (2013) 543–548.
[125] M. Karaman, L. Pai-Chi, M.O. Donnell, Synthetic aperture imaging for small scale systems, IEEE Trans. Ultrason. Ferroelectr. Freq. Control 42 (3) (1995) 429–442.
[126] G. Matrone, A.S. Savoia, G. Caliano, G. Magenes, The delay multiply and sum beamforming algorithm in ultrasound B-mode medical imaging, IEEE Trans. Med. Imaging 34 (4) (2015) 940–949.
[127] M. Polichetti, F. Varray, J.C. Béra, C. Cachard, B. Nicolas, A nonlinear beamformer based on p-th root compression—application to plane wave ultrasound imaging, Appl. Sci. 8 (4) (2018) 599.
[128] F. Prieur, O.M.H. Rindal, A. Austeng, Signal coherence and image amplitude with the filtered delay multiply and sum beamformer, IEEE Trans. Ultrason. Ferroelectr. Freq. Control 65 (7) (2018) 1133–1140.
[129] C.-C. Shen, P.-Y. Hsieh, Ultrasound baseband delay-multiply-and-Sum (BB-DMAS) nonlinear beamforming, Ultrasonics 96 (2019) 165–174.
[130] T. Latychevskaia, Lateral and axial resolution criteria in incoherent and coherent optics and holography, near-and far-field regimes, Appl. Opt. 58 (13) (2019) 3597–3603.
[131] F. Gao, R. Zhang, X. Feng, S. Liu, R. Ding, R. Kishor, L. Qiu, Y. Zheng, Phase-domain photoacoustic sensing, Appl. Phys. Lett. 110 (3) (2017) 033701.

Rongkang Gao is a Postdoctoral Research Fellow at SIAT, CAS. She received her Ph.D. degree from the University of New South Wales, Australia, 2018. She joined SIAT in November 2018. Dr. Gao's research interests focus on the development and application of photoacoustic spectroscopy, and nonlinear photoacoustic technique.

Zhiqiang Xu is a Postdoctoral Research Fellow at SIAT, CAS. He received both his Ph.D. and Bachelor degree from Wuhan University of Technology, each in 2020 in Information and Communication Engineering and in 2012 in Electronic Information Engineering. His research focuses on fast photoacoustic microscopy and parallel computing.

Yaguang Ren is a Postdoctoral Research Fellow at SIAT, CAS. In 2018, she got the Ph.D. degree in bioengineering at the Hong Kong University of Science and Technology, Hong Kong, China. Her research interest includes the development of photoacoustic imaging, fluorescent microscope imaging and image processing.

Liang Song is a professor at SIAT, CAS and founding directors of The Research Lab for Biomedical Optics, and The Shenzhen Key Lab for Molecular Imaging. Prior to joining SIAT, he studied at Washington University, St. Louis and received his Ph.D. in Biomedical Engineering. His research focuses on multiple novel photoacoustic imaging technologies

Chengbo Liu is an professor at SIAT, CAS. He received both his Ph.D and Bachelor degree from Xi'an Jiaotong University, each in 2012 in Biophysics and 2007 in Biomedical Engineering. During his Ph.D. training, he spent two years doing tissue spectroscopy research at Duke University as a visiting scholar. Now he is an associate professor at SIAT, working on multi-scale photoacoustic imaging and its translational research.